REPORT DOCUMENTATION PAGE

Form Approved
OMB No. 0704-0188

PLEASE DO NOT RETURN YOUR FORM TO THE ABOVE ORGANIZATION.

1. REPORT DATE *(DD-MM-YYYY)*	2. REPORT TYPE	3. DATES COVERED *(From - To)*
04-19-2017	Journal Paper	1 Jan 2014 - 1 Aug 2016

4. TITLE AND SUBTITLE
Magnetization in the South Pole-Aitken basin: Implications for the lunar dynamo and true polar wander

5a. CONTRACT NUMBER
N/A

5b. GRANT NUMBER
N/A

5c. PROGRAM ELEMENT NUMBER
N/A

6. AUTHOR(S)
Michael Nayak, Doug Hemingway, Ian Garrick-Bethell

5d. PROJECT NUMBER
N/A

5e. TASK NUMBER
N/A

5f. WORK UNIT NUMBER
N/A

7. PERFORMING ORGANIZATION NAME(S) AND ADDRESS(ES)
Air Force Institute of Technology, 2950 Hobson Way, Wright Patterson AFB, OH 45433
UC Santa Cruz, 1156 High St, Santa Cruz, CA 95064

8. PERFORMING ORGANIZATION REPORT NUMBER
N/A

9. SPONSORING/MONITORING AGENCY NAME(S) AND ADDRESS(ES)
Air Force Institute of Technology, 2950 Hobson Way, Wright Patterson AFB, OH 45433

10. SPONSOR/MONITOR'S ACRONYM(S)
AFIT/CIP

11. SPONSOR/MONITOR'S REPORT NUMBER(S)
N/A

12. DISTRIBUTION/AVAILABILITY STATEMENT
Distribution A. Approved for public release: distribution unlimited.

13. SUPPLEMENTARY NOTES
Icarus 286 (2017) 153–192; DOI 10.1016/j.icarus.2016.09.038

14. ABSTRACT
A number of magnetic anomalies are present along the northern edge of the lunar South Pole-Aitken (SPA) basin. A variety of hypotheses for their formation have been proposed, but an in-depth study of their properties has not been performed. Here we use two different methods to invert for their source body characteristics: one that completely searches a small parameter space of less than ten uniform- strength dipoles per anomaly, and another that uses grids of hundreds of dipoles with variable magneti- zation strengths. Both methods assume uniform magnetization directions at each anomaly and with one exception, produce nearly the same results. We introduce new Monte Carlo methods to quantify errors in our inversions arising from Gaussian time-dependent changes in the external field and the uncertain geometry of the source bodies. We find the errors from uncertainty in source body geometry are almost always higher. We also find a diverse set of magnetization directions around SPA, which we combine with other physical arguments to conclude that the source bodies were likely magnetized in a dynamo field. Igneous intrusions are a reasonable explanation (Purucker et al., 2012) for the directional variability, since they could be intruded over different magnetic epochs.

15. SUBJECT TERMS
NASA, USAF, planetary science, Mars, Phobos, Deimos, Moon, magnetism, magnetic anomalies, instruments, orbital dynamics, spectrometry

16. SECURITY CLASSIFICATION OF:			17. LIMITATION OF ABSTRACT	18. NUMBER OF PAGES	19a. NAME OF RESPONSIBLE PERSON
a. REPORT	b. ABSTRACT	c. THIS PAGE			MICHAEL NAYAK
UU	UU	UU	NONE	40	19b. TELEPHONE NUMBER *(Include area code)* 808-891-7727

Reset

Standard Form 298 (Rev. 8/98)
Prescribed by ANSI Std. Z39.18
Adobe Professional 7.0

Icarus 286 (2017) 153–192

Contents lists available at ScienceDirect

Icarus

journal homepage: www.elsevier.com/locate/icarus

Magnetization in the South Pole-Aitken basin: Implications for the lunar dynamo and true polar wander

Michael Nayak[a,b,1,*], Doug Hemingway[a,2], Ian Garrick-Bethell[a,c]

[a] Department of Earth & Planetary Sciences, University of California Santa Cruz, 1156 High Street, Santa Cruz, CA, 95064, USA
[b] Red Sky Research, LLC, 67 Northland Meadows Dr., Edgewood, NM, 87105, USA
[c] School of Space Research, Kyung Hee University, Yongin-si, Gyeonggi-do 446-701, Republic of Korea

ARTICLE INFO

Article history:
Received 1 February 2016
Revised 8 September 2016
Accepted 22 September 2016
Available online 14 October 2016

Keywords:
Moon
Magnetic fields
Impact processes

ABSTRACT

A number of magnetic anomalies are present along the northern edge of the lunar South Pole-Aitken (SPA) basin. A variety of hypotheses for their formation have been proposed, but an in-depth study of their properties has not been performed. Here we use two different methods to invert for their source body characteristics: one that completely searches a small parameter space of less than ten uniform-strength dipoles per anomaly, and another that uses grids of hundreds of dipoles with variable magnetization strengths. Both methods assume uniform magnetization directions at each anomaly and with one exception, produce nearly the same results. We introduce new Monte Carlo methods to quantify errors in our inversions arising from Gaussian time-dependent changes in the external field and the uncertain geometry of the source bodies. We find the errors from uncertainty in source body geometry are almost always higher. We also find a diverse set of magnetization directions around SPA, which we combine with other physical arguments to conclude that the source bodies were likely magnetized in a dynamo field. Igneous intrusions are a reasonable explanation (Purucker et al., 2012) for the directional variability, since they could be intruded over different magnetic epochs. However, the directional variability also implies either surprisingly large amounts of true polar wander or a dynamo not aligned with the lunar spin axis. We also explore the possibility that true polar wander caused by the SPA impact could allow iron-rich SPA ejecta to record a diverse set of magnetic field directions. Some of this material may have also become "sesquinary" ejecta and re-impacted across the Moon on 10^4–10^6 year timescales to capture such changes. No completely satisfactory answer emerges, except that the dipole-axis of the lunar dynamo may have been variable in direction.

Published by Elsevier Inc.

1. Introduction

The South Pole-Aitken (SPA) Basin is the Moon's largest and oldest well-defined basin (Garrick-Bethell and Zuber, 2009). It is also the site of the largest grouping of magnetic anomalies on the Moon (Purucker, 2008). Initially discovered by the Apollo 15 subsatellite (Coleman et al., 1972), the origin of these features remains unknown. Over the last 20 years, three dominant hypotheses for their formation have emerged. The first is that ejecta from the Imbrium and Serenitatis basins has accumulated at their antipodes, which fall within the SPA basin (Hood and Huang, 1991;Lin et al., 1998; black crosses in Fig. 1). This antipodal ejecta then attains a remanent magnetization from either a dynamo field, or a field related to the impact event (Hood and Artemieva, 2008). The second hypothesis is that the anomalies arise from subsurface dikes that cooled in a dynamo field (Purucker et al., 2012). The third is that iron-rich material derived from the SPA impactor cooled in a dynamo field (Wieczorek et al., 2012). Determining which, if any, of these hypotheses are true would have implications for understanding the nature and history of the lunar dynamo.

Despite the importance of these anomalies in understanding lunar magnetism, no detailed studies of the source body characteristics have been performed. Purucker et al. (2012) modeled one of the anomalies within SPA as a series of vertically magnetized dikes, and estimated their magnetization strength. Global studies of lunar magnetic anomalies have neglected the SPA region (Arkani-Hamed and Boutin, 2014; Takahashi et al., 2014), because of the

* Corresponding author at: Department of Earth & Planetary Sciences, University of California Santa Cruz, 1156 High Street, Santa Cruz, CA, 95064, USA
E-mail addresses: mnayak@ucsc.edu, nayak@redskyresearch.org (M. Nayak).
[1] Formerly: NASA Ames Research Center, Planetary Systems Branch (SST), Moffett Field, CA, 94035, USA, Now at: Maui High Performance Computing Center, Air Force Research Laboratory (AFRL)
[2] Now at: Miller Institute for Basic Research in Science, Department of Earth & Planetary Science, University of California Berkeley, Berkeley, CA, USA

http://dx.doi.org/10.1016/j.icarus.2016.09.038
0019-1035/Published by Elsevier Inc.

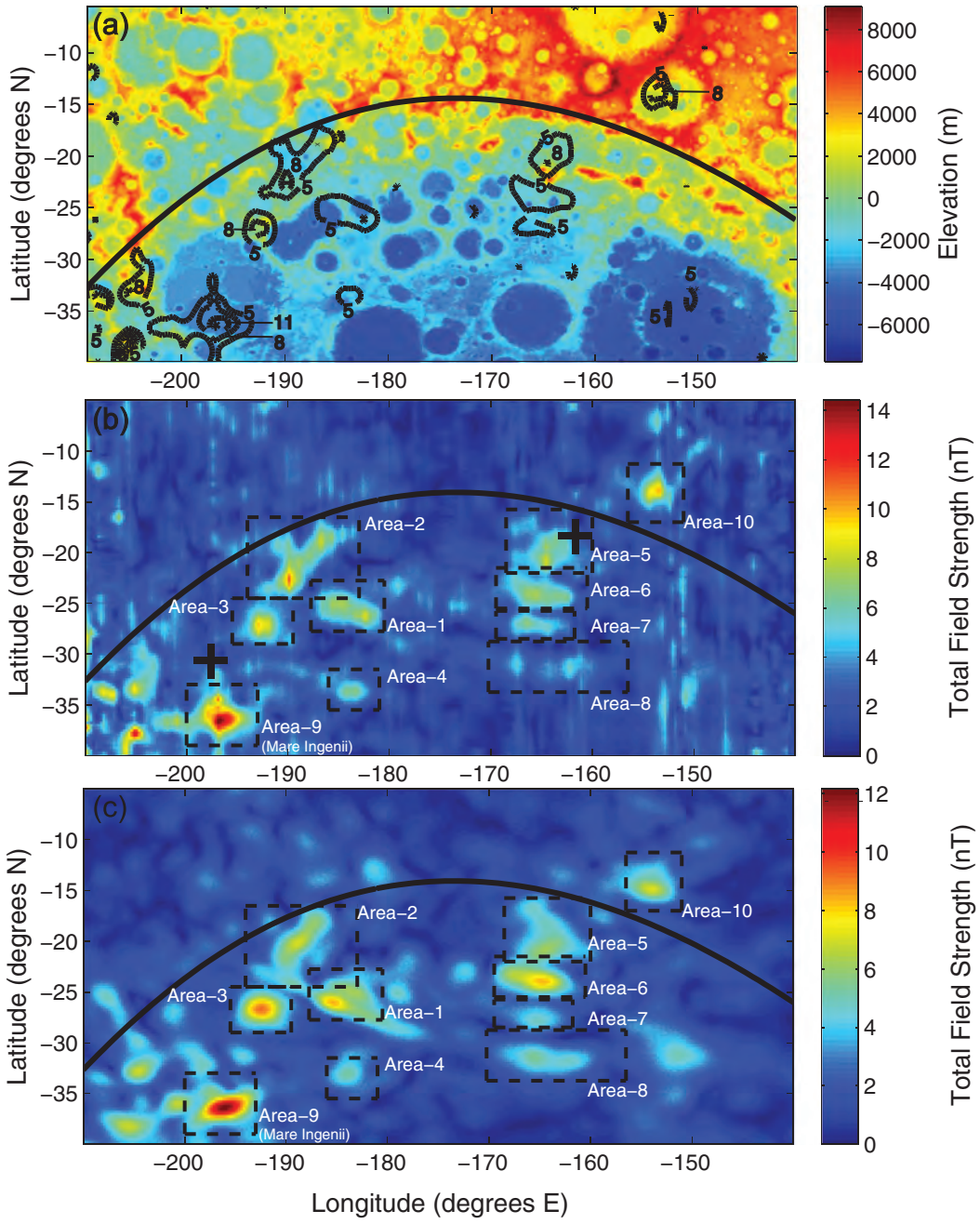

Fig. 1. Lunar South Pole-Aitken basin study areas. The SPA rim (thick black line) is from Garrick-Bethell and Zuber (2009). (a) Magnetic contours superimposed over LOLA topography data (contours are taken from the map in part b). Contours shown are 5, 8 and 11 nT; (b) magnetic field map with study areas highlighted (dashed black lines). Magnetic field data are from the Kaguya spacecraft magnetometer measurements taken on day 96 in 2009; at a mean altitude of 39.4 km. Black crosses indicate the location of the Imbrium (west) and Serenitatis (east) basin antipodes. (c) Magnetic field map derived from a spherical harmonic model evaluated at 39.4 km (Purucker and Nicholas, 2010). Study areas are highlighted. We refer to areas 1–3 as the northwestern cluster, and areas 5–8 as the eastern stripes.

complicated field structure in the region. Using a method they refer to as surface vector mapping, Tsunakawa et al. (2014) calculated the statistics of the declination of the field over the anomalies at SPA. Based on the distribution of declinations, they found evidence that the source bodies are horizontally elongated in the east-west direction. While they also estimated the magnetization direction and magnetic paleopole from the anomaly centered on the Leibnitz crater within SPA, they did not estimate the source body characteristics of any of the larger magnetic anomalies that characterize the region.

Here, we will show that many individual anomalies can be identified within SPA. We use software that can readily generate and compare magnetic field maps from all available observations, helping us avoid spurious or poorly defined magnetic anomalies that may have complicated other efforts to study the region. Comparisons with a spherical harmonic model of the magnetic field (Purucker and Nicholas, 2010) provide a further test of consistency. We will show that the source body magnetization directions offer a key test for their formation hypotheses, and we make a substantial effort to characterize the uncertainty in these directions. The paper is organized as follows: Section 2 presents our methods, including uncertainty estimation, Section 3 presents our results, and in Section 4, we discuss possible origins of the observed diversity in magnetization directions. We consider impact and dynamo

origins for these anomalies, and attempt to explain their directional variability with secular variation, a dynamo not aligned with the lunar spin axis, and both long and short-timescale true polar wander. Finally, Section 5 contains our conclusions.

2. Methods

2.1. Data sources

We use magnetometer data from two independent sources: Lunar Prospector (LP-MAG) and SELENE/Kaguya (K-MAG). The Lunar Prospector fluxgate magnetometer measured the vector magnetic field at up to 18 Hz and transmitted its measurements at a reduced resolution of 9 Hz. Level 1B LP-MAG data are obtained from the NASA Planetary Data System (ppi.pds.nasa.gov). The SELENE/Kaguya spacecraft used a tri-axial fluxgate magnetometer with a sampling rate up to 32 Hz. K-MAG magnetometer data are obtained from the SELENE data archives (l2db.selene.darts.isas.jaxa.jp). The cadence of measurements used in this study is 0.2 Hz for LP-MAG and 0.25 Hz for K-MAG. Topography data are from the Lunar Orbiter Laser Altimeter (LOLA) (Smith et al., 2010) (pds-geosciences.wustl.edu).

To best capture the Moon's crustal field, all data used for analysis were collected in either the lunar wake or while the Moon was in the Earth's magnetotail (hereafter referred to as wake and tail data), avoiding distortions caused by the solar wind noted by Halekas et al. (2008); Kurata et al. (2005). Tail datasets specifically exclude epochs during which plasma sheet disturbances were noted (Halekas et al., 2012). Consecutive orbits are ~1° in longitude apart. At 0.2 Hz, successive magnetometer measurements are separated by ~8 km in the latitudinal direction. All data used in this study are from the final months of Lunar Prospector in 1999 and Kaguya in 2009, when measurements were taken at observation altitudes below 50 km.

2.2. Data processing and anomaly identification

Details on the generation of magnetic field maps used in this paper (e.g. Fig. 8) are after Hemingway and Garrick-Bethell (2012), summarized here for completeness. After subtracting the background field (taken to be the mean field across each orbit segment spanning the region of interest), the remaining fields are assumed to be due to crustal sources. Data from consecutive orbits are combined and fit to square meshes using Delaunay triangulation, with a grid spacing of $0.25° \times 0.25°$ ($7.6\,km \times 7.6\,km$ equatorial). This spacing is finer than the spacing between observations (e.g., ~8 km latitude, ~30 km longitude for LP-MAG), ensuring no loss of signal variation during grid generation. Orbit segments that visually appear distorted by transient magnetic field oscillations, despite these efforts, are discarded. Gaps in spacecraft coverage, if any, can be seen in magnetic field maps, as the spacecraft measurement locations are shown in all figures (e.g. Fig. 8, white points).

To analyze the northern SPA region, we divide the strongest magnetic anomalies into ten study areas (Fig. 1). We choose anomalies whose Kaguya and LP magnetic field maps are consistent with maps from a spherical harmonic model of the field (Purucker and Nicholas, 2010), which can be seen by comparing Fig. 1b and c. Anomalies that were not consistent with this model or showed artifacts of external disturbances were not used. Areas 1 and 2 encompass two approximately linear and perpendicular magnetic features; in their vicinity is area 3, also in proximity to the Van de Graaff crater (Dyal et al., 1974). Area 1 is very similar to the area modeled by Purucker et al. (2012). Together, we refer to Areas 1–3 as the northwestern cluster. Area 9 is to the southwest of these areas and is associated with the "swirl" albedo anomalies at Mare Ingenii (Blewett et al., 2011; Kramer et al., 2011). Area 4 is an isolated anomaly to the southeast of areas 1–3. Areas 5–8 are roughly east-west trending linear features found to the east of these study areas, and together we refer to them as the eastern stripes. The anomalies at areas 1 and 8 appear connected in some maps of the magnetic field (Purucker et al. 2012). Finally, we also define area 10, interesting because it falls outside the basin's outer topographic rim (Garrick-Bethell and Zuber, 2009).

We divide all data in this paper by the day of observation, such that each dataset for a given anomaly is collected at approximately the same altitude. The datasets may be referenced to the day on which they were collected, e.g., 1999 day 172 (LP-MAG; read as 99172) or 2009 day 123 (K-MAG; read as 09123). Figs. 2 and 3 show an overview of the total magnetic field maps created for all observation days used for all study areas; Appendix A shows details of magnetic inversions for all these areas (see Sections 2.3 and 2.4). Supplementary Appendix B shows maps of the total field for all available days that were considered, but not used.

2.3. Inversion algorithm 1: defined dipoles, constant magnetization (DD-CM)

To assess the robustness of our results, we use two different algorithms to invert for source body characteristics. Both are regressions to find the least squared error. The first completely searches a parameter range using manually placed dipoles as the source bodies. The regression parameter space varies burial depth in km, magnetic dipole moment in Am^2, magnetic dip (inclination) in degrees downward from the horizontal, and declination in degrees clockwise from north. All dipoles in a given study area are constrained to be at the same depth, moment and direction. Source dipole positions (latitude θ_s and longitude ϕ_s) are placed manually by the user at locations where the magnetic field strength is greatest according to our maps. We refer to this henceforth as the defined dipoles, constant magnetization (DD-CM) algorithm. As we will show, the ability to completely search a parameter space at relatively fast computation speeds gives this algorithm some advantages when uncertainties must be estimated.

The depth is allowed to vary between 1 km and 99 km in steps of 0.25 km, and the dipole magnetic moment between $10^{11}\,Am^2$ and $10^{14}\,Am^2$ in steps of $2.5 \times 10^{11}\,Am^2$. Depth solutions are further constrained to be no shallower than the deepest negative topography in a given study area, ensuring that all solutions lie beneath the lunar surface; depth is measured against a reference sphere of 1737.4 km (Smith et al., 2010). The magnetic inclination is allowed to vary from −90° to +90° in steps of 1° and declination from −180° to +180° in steps of 1°.

For n field measurements inside a given study area, the difference between the model and the data is computed. We minimize the root mean square (RMS) total error of the i^{th} east (δB_{east}), north (δB_{north}) and radial (δB_{radial}) component errors, δB_{total}, as:

$$(\delta B_{total})_{RMS} = \sqrt{\frac{1}{n}\sum_{i=1}^{n}\left(\delta B_{i,\ east}{}^2 + \delta B_{i,\ north}{}^2 + \delta B_{i,\ radial}{}^2\right)} \qquad (1)$$

This quantity is then ranked in decreasing order of total error to find the best-fit magnetic characteristics.

2.4. Inversion algorithm 2: gridded dipoles, variable magnetization (GD-VM)

We test the validity of our inversion results using an alternative, more objective approach, at the expense of exploring a much larger parameter space. Instead of placing dipoles manually, we establish a $0.25° \times 0.25°$ grid of dipoles covering the entire study area (Hemingway and Garrick-Bethell, 2012; Nicholas et al., 2007).

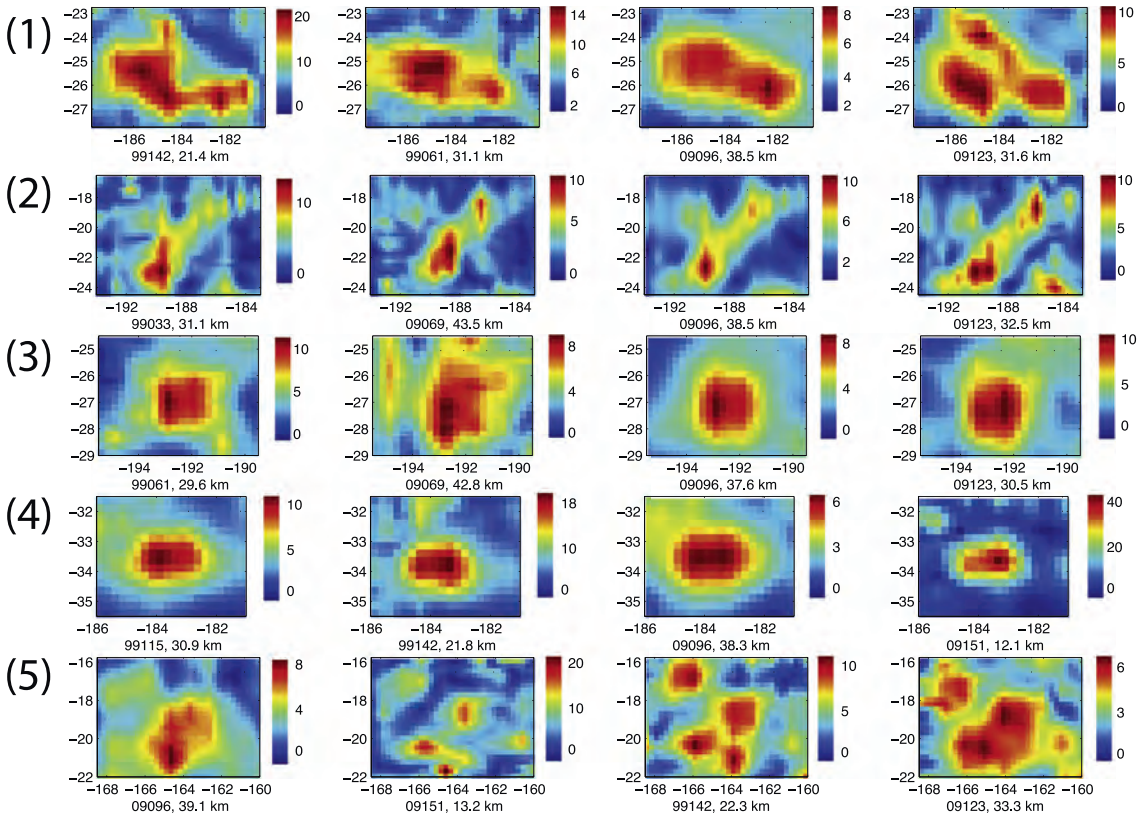

Fig. 2. Overview of all datasets used for SPA areas 1–5. Maps show total field strength in units of nanotesla, as a function of latitude and longitude (degrees). The number in parentheses denotes a study area from Fig. 1. Mean measurement altitudes are shown. Data collection days may be read in the format YY-DDD, e.g., 09123 is 2009 day 123, and so on.

All dipoles are again constrained to be at the same depth, inclination and declination. Unlike the first algorithm, however, the magnetic moment is allowed to vary among the dipoles. This creates a large $m+3$ parameter space, where m is the number of dipoles; Table 1 lists the number of gridded dipoles for each study area, which ranges from 320–1408. The solution is then found via a genetic search algorithm that minimizes the RMS error (for details, see Hemingway and Garrick-Bethell, 2012). The algorithm evolves through "generations" to progress toward a better fit (smaller error) to the data. However, the evolutionary nature of the algorithm does not guarantee optimality of the solution. We refer to this henceforth as the gridded dipoles, variable magnetization (GDVM) algorithm. The grid of best-fit magnetic moments found by this method, ranging across several orders of magnitude at each anomaly, can be seen in Supplementary Appendix C, which shows representative results for each study area.

2.5. Uncertainty estimation for magnetization directions

Error in our regressions arises from: *(1)* time-variable contributions to the measured field due to non-crustal fields or instrument noise, *(2)* the ideal assumption that the source is uniformly magnetized in the same direction, and *(3)* the simplified geometry of our source models, even if the assumption of unidirectional magnetization were completely true.

2.5.1. Time-variable fields

One method to account for the first source of error is to report the set of solutions with an RMS error equal to or less than the uncertainty in the magnetic field measurements (Parker, 1991). The range of magnetization directions in this set then defines the error in the best-fit direction. The drawback of this method is that the use of the field's uncertainty is arbitrary. For example, at different observation altitudes, the magnitude of the RMS error for the best-fit solution will vary, such that the measurement uncertainty will have a different impact on the size of the set of solutions that represent the error. More importantly, as we show below, the set of allowable solutions suggested by propagating Gaussian measurement noise (or external field oscillations) of a given magnitude through the inversion is often small compared with the size of the set of solutions contained by an RMS error of equal magnitude. That is, using the uncertainty in the field measurement to define the allowable solution set can overestimate the error in the regression.

To demonstrate this effect, we simulate the effect of Gaussian measurement noise in each of the 45 regressions we perform (all maps shown in Figs. 2 and 3). Before doing so, we first estimate the characteristic noise magnitude. For both LP-MAG and K-MAG, the instrument noise is <0.1 nT, such that the dominant source of error arises from fluctuations in the interplanetary magnetic field (IMF) rather than the instrument. To estimate a characteristic amplitude of the oscillations in the IMF over the timescale of observation at one magnetic anomaly, while in the wake or magnetotail, one would ideally examine the time-dependent oscillations just prior to flying over the anomaly of interest. However, there is no simple way to separate oscillations arising from small-scale crustal fields and time dependent fields. As a rough proxy, we can examine the field variations over the Mare Imbrium region while the Moon is in the wake. Since the Imbrium region is known to have the lowest amount of crustal magnetism anywhere on the

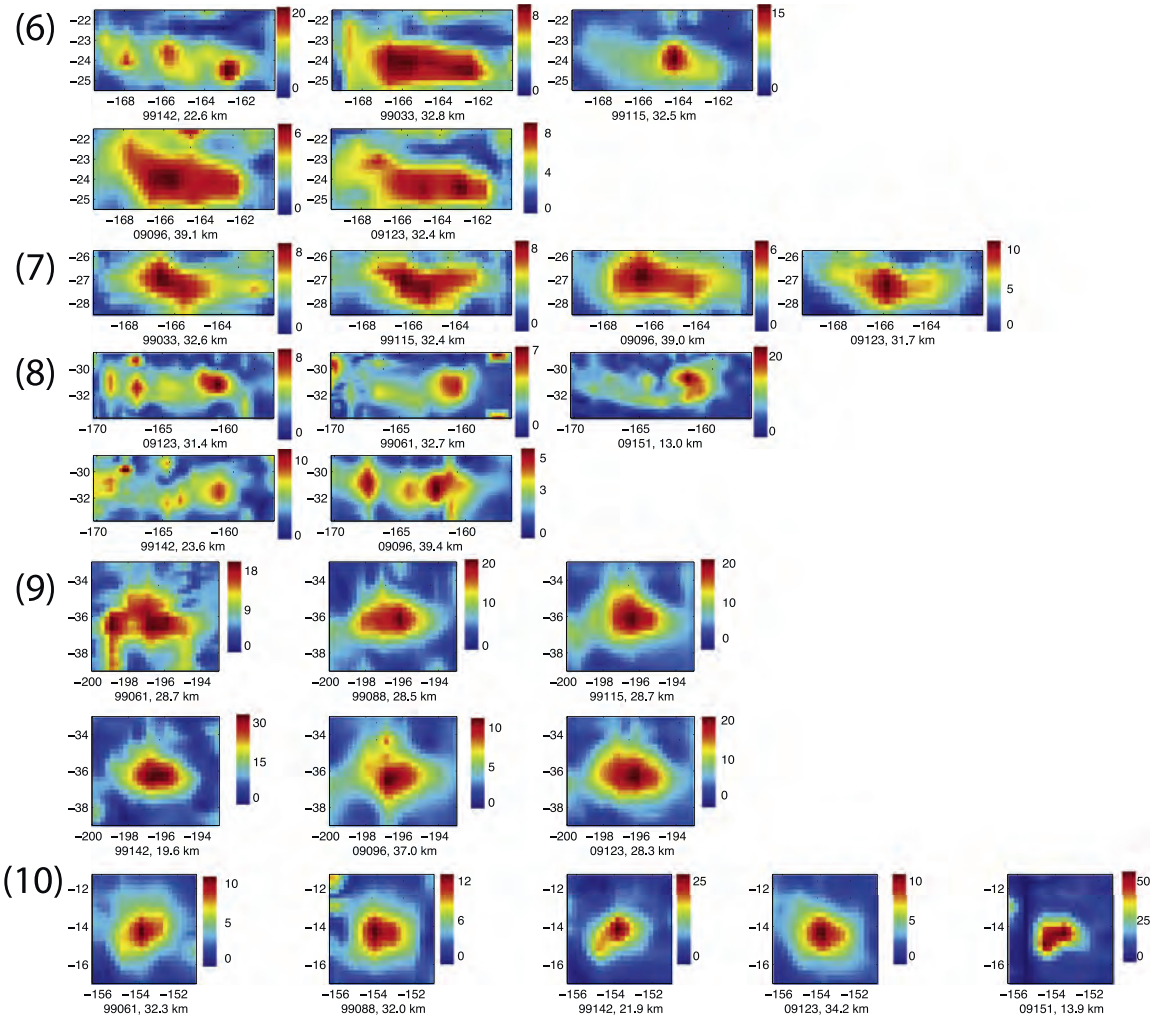

Fig. 3. Overview of all datasets used for SPA areas 6–10. Maps show total field strength in units of nanotesla, as a function of latitude and longitude (degrees). The number in parentheses denotes a study area from Fig. 1. Mean measurement altitudes are shown. Data collection days may be read in the format YY-DDD, e.g., 09123 is 2009 day 123, and so on.

Moon (Mitchell et al., 2008; Tsunakawa et al., 2014), magnetic field oscillations there are most likely to represent only time dependent effects. We find that the standard deviations of the field at Imbrium are 0.07 nT and 0.13 nT for two representative days (Fig. 4). However, to be conservative, we use an order of magnitude higher standard deviation of 1 nT as the characteristic value. Takahashi et al. (2014) make a similar (1 nT) assumption about the magnitude of external field contributions.

Next, to simulate the effect of typical time-dependent fields in our DD-CM regressions, we added random Gaussian noise with a standard deviation of 1 nT to each field component (east, north, radial) for all 45 datasets. An example is shown in Fig. 5. Note that we are assuming that the noise at each measurement point is uncorrelated with the previous measurement point. Our assumption is only valid if oscillations in the IMF occur on timescales faster than the time between measurements (5 seconds for LP data, and 4 seconds for Kaguya data). Future work will determine the dependence of our error estimates on a variety of correlation timescales, and better determine the typical timescale of time-dependent field oscillations.

For each of the 45 datasets (Figs. 2 and 3), we generated 20 sets of noise-added data. Assuming the best-fit directions follow a Fisher distribution (the Fisher distribution gives the probability of finding a direction within an angular area from the true mean; Fisher, 1953), their angular standard deviations and Fisher distribution precision parameters k, were then obtained from each set of 20 simulations. The mean k value across all altitudes within a study area was then used as the final estimate of the uncertainty from time-dependent fields for that study area (for example, for area 1, which uses data from four different altitudes, four different k values were averaged together). The ability to simulate the effect of noise in this manner represents an advantage of the DD-CM method, which has a faster computation time compared to the GD-VM method.

We find that the angular standard deviation in best-fit direction associated with 1 nT noise is always smaller than the set of directions permitted when using an error threshold of 1 nT. For example, the best-fit RMS error for area 1, 09096 (Fig. 5) is 2.4 nT, which is already greater than the ~1 nT uncertainty we estimate for the field (this inequality is true for nearly all inversions in this study). The set of solutions that are allowed by considering 1 nT additional RMS error (total residual error 3.4 nT) produces ~30° of uncertainty in the best-fit magnetization direction (Fig. 6). In contrast, Fig. 6 also shows that adding 1 nT Gaussian noise to the observations via the above method only produces an angular standard deviation of 5° in the best-fit direction. The smaller size of the effect of simulated Gaussian noise is true in all of our regressions.

Table 1
Lunar Prospector (LP) and Kaguya (KG) datasets used for inversions, with best-fit parameters found using both the DD-CM and GD-VM algorithms. Mean observational altitude, data day and site latitude and longitude are shown. GD-VM dipoles column indicates the number of gridded dipoles used for the GD-VM simulation. Estimated magnetizations from both algorithms are shown (see text for details). The merged row for each study area shows the best-fit parameters obtained from merged data at all altitudes using the GD-VM algorithm. Highlighted rows correspond to figures shown in the main text (Figs. 8–17); GD-VM dipole maps for these datasets are also shown in Supplementary Appendix C. Best-fit figures for non-highlighted rows are in Appendix A.

							DD-CM algorithm					GD-VM Algorithm				
Study Area	Spacecraft	Year	Day	Latitude (deg N)	Longitude (deg E)	Alt (km)	Depth (km)	Moment (10^{12} Am^2)	Inc (deg)	Dec (deg)	Mag (A/m)	Dipoles	Depth (km)	Inc (deg)	Dec (deg)	Mag (A/m)
1	LP-MAG	1999	142	−25	−184	22.4	25	8.4	13	−123	0.12	580	5	18	−128	0.70
	LP-MAG	1999	61	−25	−184	32.3	24	6.4	32	−116	0.09	580	5	22	−128	0.62
	K-MAG	2009	96	−25	−184	39.4	36	11.0	42	−132	0.06	580	26	30	−126	0.12
	K-MAG	2009	123	−25	−184	33	37	6.4	20	−114	0.11	580	14	20	−116	0.24
	Merged											580	6	19	−123	0.42
2	LP-MAG	1999	33	−20	−188	32.8	46	21.0	36	21	0.06	1408	21	11	−71	0.20
	K-MAG	2009	69	−20	−188	44.7	37.5	26.0	29	−129	0.06	1408	39	5	−54	0.10
	K-MAG	2009	96	−20	−188	39.4	40	15.0	26	−135	0.07	1408	38	7	−52	0.11
	K-MAG	2009	123	−20	−188	33	40	20.0	32	−141	0.07	1408	26	7	−53	0.16
	Merged											1408	12	8	−59	0.14
3	LP-MAG	1999	61	−27	−192	32.3	47	19.0	31	1	0.08	432	21	20	3	0.16
	K-MAG	2009	69	−27	−192	44.7	55	62.0	32	−8	0.10	432	27	13	−1	0.16
	K-MAG	2009	96	−27	−192	39.4	49.5	18.0	49	4	0.07	432	23	27	−8	0.13
	K-MAG	2009	123	−27	−192	33	48	17.0	49	2	0.06	432	23	21	2	0.13
	Merged											432	11	25	−8	0.15
4	LP-MAG	1999	115	−33	−183	32.3	28	6.4	−64	−46	0.06	320	24	−55	−56	0.09
	LP-MAG	1999	142	−33	−183	22.4	40.5	12.0	−73	−89	0.07	320	13	−52	−50	0.20
	K-MAG	2009	96	−33	−183	39.4	28	6.2	−69	−23	0.06	320	24	−70	−28	0.08
	K-MAG	2009	151	−33	−183	13.7	23.5	5.7	−82	86	0.06	320	8	−62	−42	0.30
	Merged											320	9	−85	−73	0.17
5	K-MAG	2009	96	−19	−165	39.4	32.5	11.0	−33	−16	0.06	850	24	−23	−23	0.15
	K-MAG	2009	151	−19	−165	13.7	55	34.0	−24	−12	0.12	850	25	−34	−33	0.17
	LP-MAG	1999	142	−19	−165	22.4	46	21.0	−29	−23	0.09	850	26	−30	−33	0.14
	K-MAG	2009	123	−19	−165	33	38.5	7.9	−56	6	0.06	850	28	−36	−25	0.11
	Merged											850	12	−30	−39	0.14
6	LP-MAG	1999	142	−24	−165	22.4	46	23.0	47	−38	0.10	576	23	50	−28	0.16
	LP-MAG	1999	33	−24	−165	32.8	55	33.0	49	24	0.08	576	31	39	53	0.13
	LP-MAG	1999	115	−24	−165	32.3	55	30.0	41	−8	0.08	576	21	47	18	0.16
	K-MAG	2009	96	−24	−165	39.4	46	22.0	49	31	0.07	576	32	31	−21	0.12
	K-MAG	2009	123	−24	−165	33	55	21.0	43	−14	0.08	576	34	38	−25	0.11
	Merged											576	12	43	15	0.14
7	LP-MAG	1999	33	−27	−165	32.8	55	22.0	35	−160	0.09	341	26	28	−132	0.15
	LP-MAG	1999	115	−27	−165	32.3	41.5	12.0	45	−180	0.07	341	25	38	159	0.12
	K-MAG	2009	96	−27	−165	39.4	24.5	8.0	46	152	0.08	341	21	34	155	0.14
	K-MAG	2009	123	−27	−165	33	37	11.0	40	131	0.07	341	24	34	143	0.12
	Merged											341	14	39	165	0.13
8	K-MAG	2009	123	−31	−164	33	25.5	6.9	2	146	0.05	1100	39	−3	−131	0.08
	LP-MAG	1999	61	−31	−164	32.3	46	21.0	1	−172	0.03	1100	45	3	134	0.06
	K-MAG	2009	151	−31	−164	13.7	25	5.9	−17	138	0.05	1100	13	0	123	0.31
	LP-MAG	1999	142	−31	−164	22.4	55	20.0	−17	−128	0.04	1100	36	−6	−119	0.10
	K-MAG	2009	96	−31	−164	39.4	28	7.8	−1	−162	0.03	1100	46	−3	−132	0.07
	Merged											1100	13	−1	−119	0.12
9	LP-MAG	1999	61	−36	−198	32.3	29.5	26.0	1	119	0.16	672	7	−4	145	0.52
	LP-MAG	1999	88	−36	−198	32.2	34	37.0	−12	146	0.13	672	9	−11	162	0.43
	LP-MAG	1999	115	−36	−198	32.3	25	30.0	−6	139	0.14	672	7	−8	141	0.49
	LP-MAG	1999	142	−36	−198	22.4	22.5	17.0	−2	144	0.18	672	4	−5	153	0.95
	K-MAG	2009	96	−36	−198	39.4	26	23.0	−5	125	0.16	672	7	−8	141	0.41
	K-MAG	2009	123	−36	−198	33	23.5	15.0	−5	135	0.19	672	5	−3	143	0.65
	Merged											672	4	−7	146	0.58
10	LP-MAG	1999	61	−14	−153	32.3	36	25.0	34	−180	0.05	506	15	15	156	0.20
	LP-MAG	1999	88	−14	−153	32.2	20.5	8.3	32	166	0.10	506	12	11	−167	0.23
	LP-MAG	1999	142	−14	−153	22.4	21	17.0	29	−175	0.06	506	5	14	−174	0.56
	K-MAG	2009	123	−14	−153	33	19	15.0	21	−172	0.06	506	5	10	−172	0.50
	K-MAG	2009	151	−14	−153	13.7	16	14.0	25	−168	0.07	506	4	10	−155	0.87
	Merged											506	4.5	13	−160	0.47

2.5.2. Non-uniform magnetization direction

The second contribution to error is the non-uniform magnetization directions in the source bodies. However, it is impossible to make any inferences about the magnetization if we permit the infinite number of possible source magnetizations with mixed directions. Therefore we must at least assume that the source is uniformly magnetized. We attempt to mitigate this effect by selecting small, well-defined anomalies (Fig. 1). Of course, if non-uniformity dominates the source of error then these regression results are less meaningful.

2.5.3. Source body geometry

Finally, we address what is likely the dominant source of uncertainty: the complex geometry of the magnetic source bodies compared to our simplified models. We do this in two ways. The first is to compute the best-fit magnetization separately for different altitude datasets at each anomaly, instead of fitting to a merged altitude dataset. Data from different altitudes display a diversity of magnetic field morphologies, as field strength decays with altitude (which ranges in this study from 13–46 km). Hence, each altitude will lead to different choices of dipole locations for the

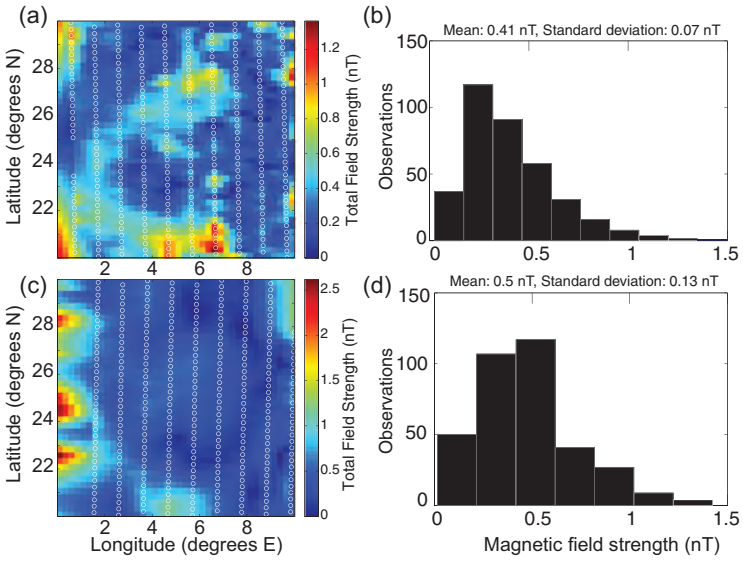

Fig. 4. Magnetic field maps and histograms of field strength at eastern Mare Imbrium in the lunar wake. Panels (a) and (c) are magnetic field maps at Imbrium using LP-MAG observation days 118 and 131 in 1999, respectively. White dots indicate observation locations. The mean observation altitude for day 118 is 31.3 km and 29.8 km for day 131. Panels (b) and (d) are corresponding histograms of the strength of the total magnetic field.

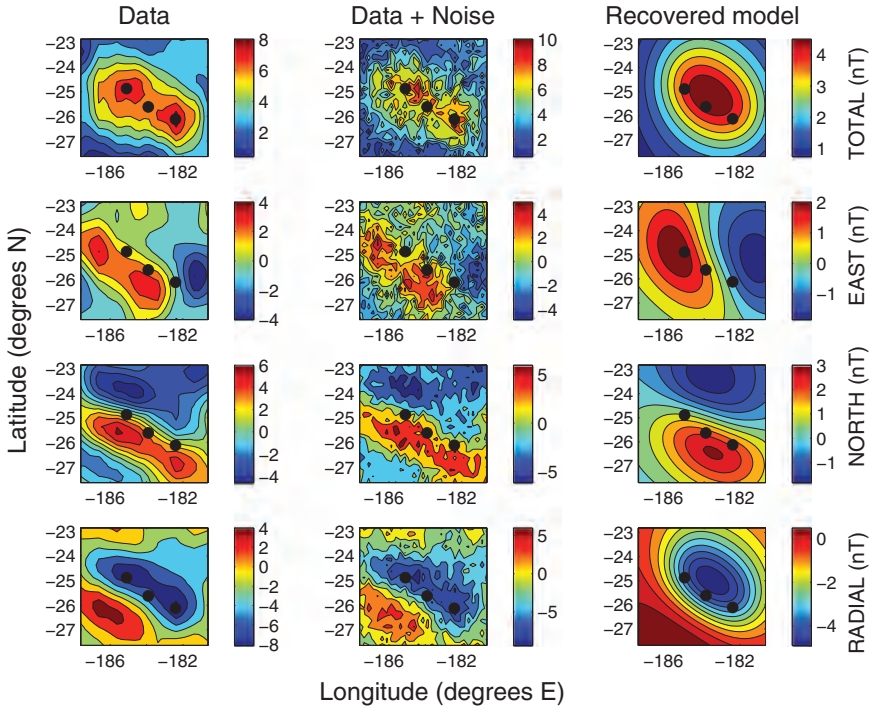

Fig. 5. Error estimation method for time-variable (non-crustal) magnetic fields. Kaguya magnetic field data for area 1, 2009 day 96 (left column), the effect of random noise with a standard deviation of 1 nT added to that data (middle column) and one of our Monte Carlo trial regressions for the depth, moment and direction values for data + noise with the DD-CM algorithm (right column). Dipole source geometry is identical to the placement in Fig. 8 (black dots).

DD-CM algorithm; for example, compare Fig. 8 to Figures A-1 to A-3 (Appendix A). This variability is an advantage, as it allows us to probe the sensitivity of our results to source geometry, with the spread in the best-fit magnetization directions representing the measure of uncertainty (this advantage will be particularly obvious for area 2, which exhibits bimodal error minima in its error space). This is analogous to the practice in paleomagnetism of sampling a single rock formation multiple times at different sites (Irving, 1964). Because each measured direction at each altitude is independently calculated we can also assign a 95% confidence interval to the mean direction from all altitudes (Butler, 1998). In practice, we combine the directions obtained from both the DD-CM and GD-VM algorithms to calculate the final mean and confidence interval, even though the direction measurements for a given day are not strictly independent across the two algorithms (see Section 3). In calculating the final mean, we also include one best-fit direction obtained from the merged data at all altitudes, using the GD-VM algorithm.

The second way we account for uncertainty due to source body geometry is to explore the range in directions that are returned by displacing the nominal DD-CM algorithm dipoles for all 45 datasets. We calculate the effect of placing dipoles anywhere ran-

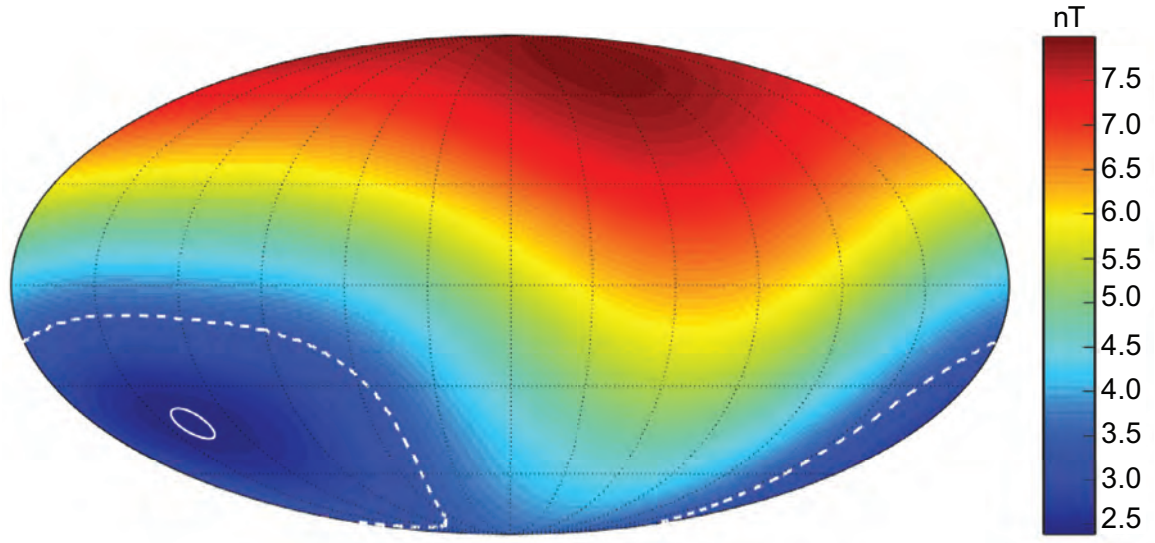

Fig. 6. RMS error map for the magnetization direction for area 1, 2009 day 96, centered at 0° inclination and 0° declination (whole-sphere Mollweide projection, in which the southern hemisphere is positive inclination, same as in Fig. 18). The small white circular contour indicates one angular standard deviation of dispersion, from Monte Carlo simulations of the addition of 1 nT Gaussian noise to observations (Fig. 5). The larger, outer white dashed contour indicates the minimum error solution plus 1 nT.

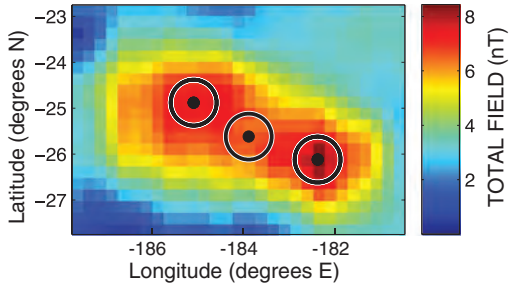

Fig. 7. Error estimation method for uncertainty in source body geometry. Black points are the nominal dipole locations for a DD-CM regression at area 1. Circles represent the allowable locations of dipoles placed randomly in our Monte Carlo simulations and are 0.5° in radius. K-MAG total field observations in the lunar wake on 2009 day 96. Compare to Fig. 8.

domly on a 0.5°-radius circle from their nominal location (Fig. 7). The value of 0.5° represents the approximate error in longitudinal uncertainty in the anomaly peak field location (orbits are spaced by approximately 1° for a given constant altitude data set). For each data set, we use 100 random placements of dipoles at any location on the defined circles and calculate the 100 best-fit magnetization directions and k values. The k values are then averaged across altitudes within an area to obtain the uncertainty from source geometry for that area. Again, this represents an advantage of the DD-CM method compared to the GD-VM method, due to the ability to modify model dipole placements and a faster computation time. We will see this advantage manifest when exploring ambiguous regression results for area 2. Finally, we note that for area 4 we use 0.25°-radius circles, due to the close proximity of the model dipoles there.

The dispersions in best-fit directions obtained from our Monte Carlo simulations for time-dependent fields (Section 2.5.1) and 0.5°-radius dipole displacements are then combined using their k values, averaged together for each area (Irving, 1964):

$$1/k_{total} = 1/k_{time-dependent,\ mean} + 1/k_{source-geometry,\ mean} \quad (2)$$

An angular standard deviation θ_{63} is then estimated by (Irving, 1964):

$$\theta_{63} \approx 81/k^{0.5} \quad (3)$$

Finally, it is linearly added to the angular 95% confidence interval obtained from the mean of the variable altitude results within a given area (conservatively assuming the Monte Carlo error does not add in quadrature, since it may be correlated).

The following is a summary of our uncertainty estimation methods:

1. Account for time-dependent external field contributions and instrument noise: Perform Monte Carlo simulations for every anomaly and altitude with the addition of 1 nT noise, and obtain mean k for the best-fit directions within an anomaly area, using the DD-CM algorithm (Fig. 5, Table 2).
2. Account for uncertainty in source geometry: Perform Monte Carlo simulations for every anomaly and altitude while altering the dipole placement, and obtain mean k for the best-fit directions within an anomaly area, using the DD-CM algorithm (Fig. 7, Table 2).
3. Combine the k values from steps 1 and 2 and obtain the angular standard deviation via Eqs. 2 and 3.
4. Account for uncertainty in source geometry by using variable altitude data, and hence variable dipole placement. Obtain a 95% confidence interval on the mean direction from the combined best-fit directions from the DD-CM and GD-VM algorithms (Table 3).
5. Linearly add the angular dispersion from step 3 to the angular 95% confidence interval from step 4 to obtain the total angular uncertainty estimate in the best-fit direction.

3. Results

3.1. Regression results

Minimum error magnetization directions are found for each Lunar Prospector and Kaguya dataset, using both the DD-CM (Section 2.3) and the GD-VM (Section 2.4) algorithms. Table 1 compiles the values of these best-fit directions. The best-fit models are shown in Figs. 8 –17 for study areas 1–10. The figures show 10 representative examples, one for each study area; Appendix A shows all results for every dataset listed in Table 1. Angular standard deviations and k for the noise-added and dipole displacement simulations are shown in Table 2 for all datasets. RMS error maps for all datasets (similar to Fig. 6) are compiled in Figs. 18 and 19;

Table 2
Uncertainty estimates for regression results from Monte Carlo simulations. Minimum RMS error recovered using the DD-CM and GD-VM algorithms for all areas and altitudes. Fisher precision parameter k, angular standard deviation θ_{63} ($\approx 81/k^{1/2}$), obtained from Monte Carlo simulations for the effects of time-dependent fields ("noise") and 0.5°-radius displaced dipoles, for the DD-CM algorithm. Highlighted rows correspond to figures shown in the main text (Fig. 8–17).

Study Area	Spacecraft	Year	Day	Min. RMS error (DD-CM) (nT)	Min. RMS error (GD-VM) (nT)	Noise simulation		Displaced dipole simulation	
						θ_{63}	Precision parameter k	θ_{63}	Precision parameter k
1	LP-MAG	1999	142	7.4	3.9	1.6	2526	7.4	120
	LP-MAG	1999	61	5.6	2.2	2.1	1474	7.3	124
	K-MAG	2009	96	2.4	1.1	5.0	264	4.2	381
	K-MAG	2009	123	6.3	2.3	2.9	774	3.8	446
2	LP-MAG	1999	33	5.9	3.1	1.5	3120	4.5	332
	K-MAG	2009	69	3.7	2.3	3.3	620	5.7	203
	K-MAG	2009	96	4.0	2.2	2.1	1542	44.1	3
	K-MAG	2009	123	5.7	3.2	1.7	2318	14.3	32
3	LP-MAG	1999	61	4.1	2.0	3.1	676	5.7	202
	K-MAG	2009	69	3.1	1.6	3.1	674	7.2	128
	K-MAG	2009	96	1.7	0.9	4.3	353	6.1	177
	K-MAG	2009	123	2.8	1.3	5.3	234	6.4	160
4	LP-MAG	1999	115	1.5	1.1	6.4	159	4.7	300
	LP-MAG	1999	142	4.4	2.0	4.2	375	5.3	232
	K-MAG	2009	96	1.1	0.8	7.2	127	5.5	219
	K-MAG	2009	151	8.1	3.7	1.9	1761	8.6	89
5	K-MAG	2009	96	2.0	1.0	5.3	232	3.7	472
	K-MAG	2009	151	9.1	4.0	1.3	3959	3.6	501
	LP-MAG	1999	142	4.6	1.9	2.0	1648	3.3	601
	K-MAG	2009	123	2.2	1.1	5.2	243	4.1	383
6	LP-MAG	1999	142	5.7	3.1	2.4	1150	15.1	29
	LP-MAG	1999	33	3.8	1.6	4.8	288	11.5	50
	LP-MAG	1999	115	3.3	2.0	4.8	283	5.3	234
	K-MAG	2009	96	2.2	1.1	7.8	109	6.9	140
	K-MAG	2009	123	2.7	1.5	4.6	308	4.4	343
7	LP-MAG	1999	33	3.1	1.6	5.0	262	4.6	311
	LP-MAG	1999	115	2.2	1.3	6.0	184	6.3	164
	K-MAG	2009	96	1.5	0.9	8.9	83	8.3	95
	K-MAG	2009	123	2.4	1.4	5.2	244	6.7	147
8	K-MAG	2009	123	2.6	1.7	4.4	347	28.0	8
	LP-MAG	1999	61	2.5	1.5	6.0	184	3.9	443
	K-MAG	2009	151	7.5	3.9	2.4	1121	36.6	5
	LP-MAG	1999	142	4.4	2.6	3.7	476	3.2	625
	K-MAG	2009	96	1.6	1.1	7.2	128	5.3	235
9	LP-MAG	1999	61	6.3	3.2	1.4	3496	4.3	352
	LP-MAG	1999	88	5.6	2.3	1.8	1999	8.1	99
	LP-MAG	1999	115	5.7	2.1	1.9	1837	9.6	71
	LP-MAG	1999	142	9.0	3.5	1.0	6997	8.5	91
	K-MAG	2009	96	4.0	1.5	2.8	853	8.1	101
	K-MAG	2009	123	4.5	1.5	1.8	2004	5.4	228
10	LP-MAG	1999	61	3.0	1.5	3.0	730	7.7	112
	LP-MAG	1999	88	3.2	1.7	7.9	104	11.9	46
	LP-MAG	1999	142	4.7	2.3	2.2	1315	10.2	63
	K-MAG	2009	123	1.9	1.3	3.9	431	7.3	124
	K-MAG	2009	151	8.0	4.2	1.2	4571	15.5	27

Table 3
Uncertainty estimates derived from using different altitude datasets. The paleolatitude, paleolongitude, value of k, and the 95% confidence circle ($\propto_{95}$) are obtained from the combined set of best-fit directions from the DD-CM and GD-VM algorithms, across all altitudes. The $\propto_{95}$ value is added to the angular uncertainty estimated by Monte Carlo simulations (equations 2 and 3, derived from mean Table 2 values) to obtain the final circular error, also shown. The distorted version of this final error circle at the paleopole is also shown (Figs. 21 and 22): the semi-axis of the ellipse along the great circle path from site to pole (dp) and semi-axis of the ellipse perpendicular to that path (dm).

Area	*Altitude averaged*		Paleolatitude	Paleolongitude	Final circular error	dp	dm
	k	α–95					
1	58.5	6.8	–34.8	84.2	12.2	7.0	13.1
2	3.3	33.9	8.5	100.4	41.0	24.0	44.3
3	38.7	8.4	46.9	165.1	15.7	9.6	17.4
4	27.8	9.9	51.8	39.1	16.4	24.5	28.4
5	33.0	9.1	68.1	104.5	13.3	8.6	15.1
6	14.5	12.4	38.0	–165.1	19.9	16.6	25.7
7	11.2	16.1	–78.5	–62.0	24.5	18.2	29.9
8	3.2	30.9	–54.2	37.8	37.1	18.7	37.3
9	50.0	5.9	–37.0	–67.6	12.6	6.3	12.6
10	25.4	9.2	–83.3	82.9	18.9	10.3	19.8

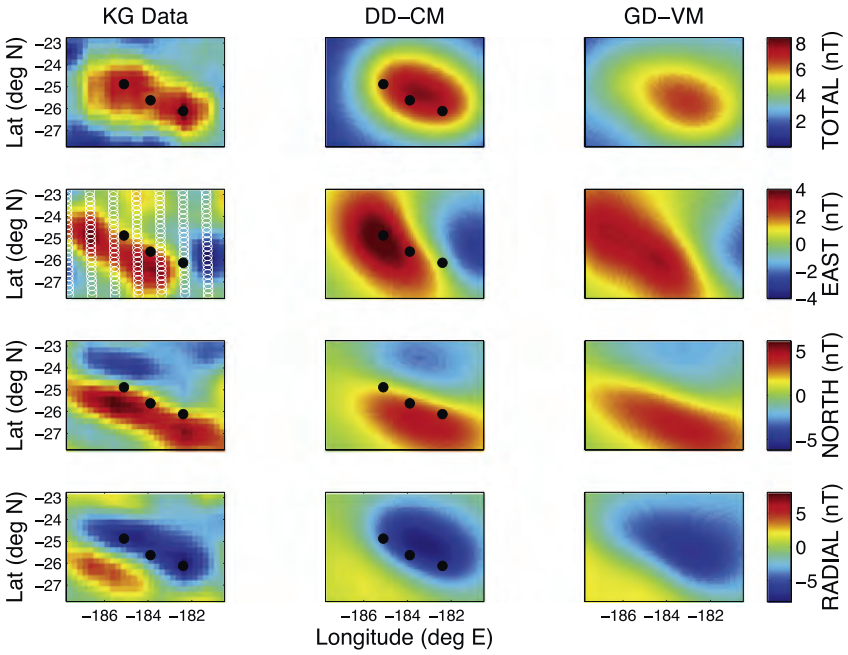

Fig. 8. Area 1 best-fit results for both inversion algorithms. (Left column) K-MAG observations in the lunar wake in 2009, day 96, at 38.5 km, compared to (middle column) a model using several manually placed dipoles of equal magnetization (DD-CM), and (right column) a grid-based model using many dipoles of variable magnetization (GD-VM). Source dipoles in the DD-CM algorithm are approximately located at maxima in the observed total field (black dots). White dots in the east panel are locations of spacecraft magnetometer measurements.

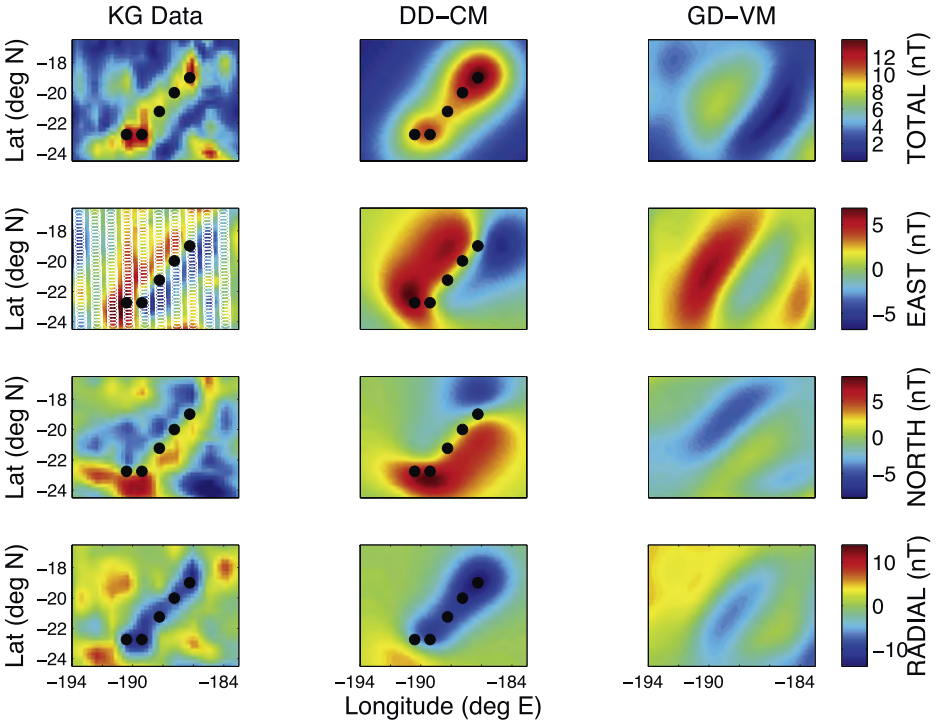

Fig. 9. Area 2 best-fit results with both inversion algorithms. Figure details are as in Fig. 8, except that magnetometer measurements are taken from K-MAG, 2009 day 123, altitude 32.5 km.

these illustrate the difference between using an arbitrary uncertainty threshold and the Monte Carlo methods employed in this work.

Fig. 20 compiles the values of the best-fit directions from the DD-CM and GD-VM algorithms. For the DD-CM algorithm, we show one standard deviation of dispersion from 1 nT noise (Fig. 20a) and one standard deviation of dispersion from displacing the model dipoles by 0.5° (Fig. 20b) (see Methods). Overall, we find the error from the uncertainty in source geometry (Fig. 20b) is usually larger than the error from the effects of time-dependent fields (Fig. 20a).

Interestingly, we find source geometry errors at areas 2 and 8 are substantially larger than for the other anomalies. The large error in area 2 arises from the existence of two nearly equal local minima in its DD-CM error map, which is not seen at any other anomaly (see Fig. 18). The two minima are approximately 110° apart. Small displacements of the dipoles from their nom-

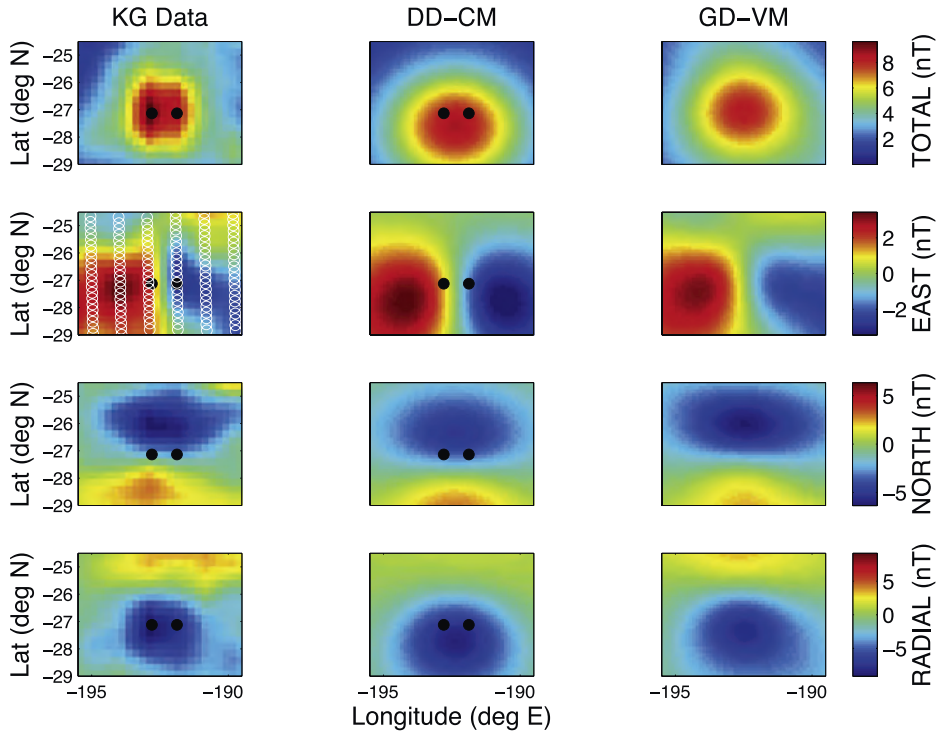

Fig. 10. Area 3 best-fit results with both inversion algorithms. Figure details are as in Fig. 8, except the altitude here is 37.6 km.

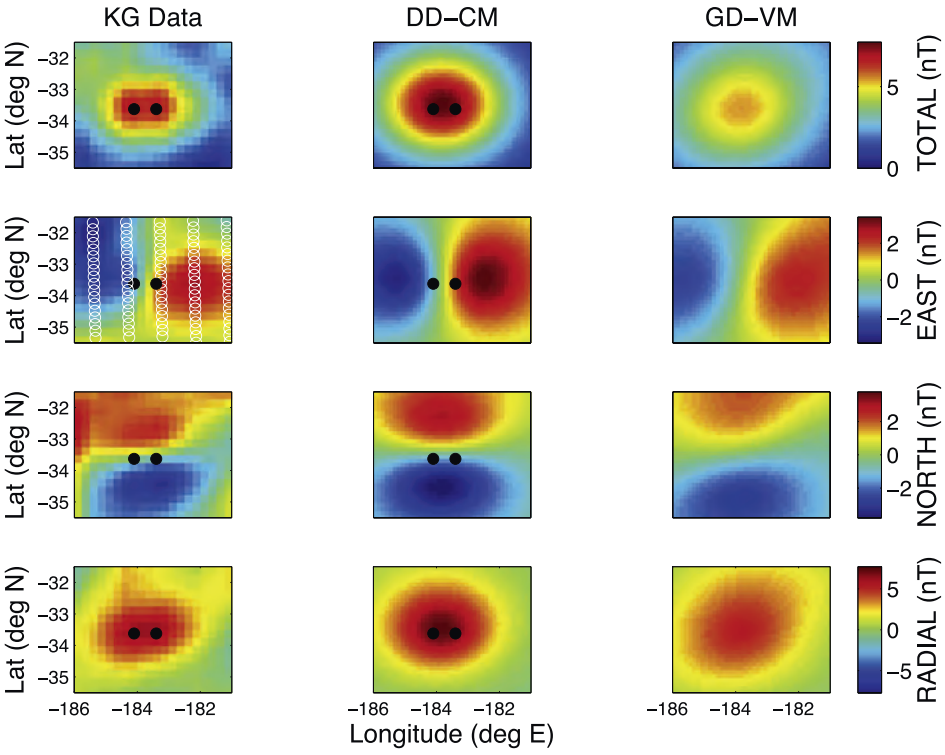

Fig. 11. Area 4 best-fit results with both inversion algorithms. Figure details are as in Fig. 8, except the altitude here is 38.3 km.

inal locations flip the best-fit solution into the other minimum, producing its large uncertainty ellipses, particularly for day 09096 (Fig. 20b). One of our four best-fit solutions (day 99033) falls in this secondary minimum. Because area 1 and 2 have slight overlap (Fig. 1), we tested if the double minima could be a result of area 1 data influencing the regression at area 2. We ran the DD-CM algorithm against data for area 2, but this time excluded spacecraft measurements over area 1. The results are not significantly different; the two minima are still seen for area 2. Using the GD-VM algorithm, one finds the best-fit directions for area 2 are approximately between the two minima found by the DD-CM algorithm (Fig. 20c), ~60° from either one. This difference between the two algorithms is the largest for any area. Further work will be required to better understand the nature of the error space at

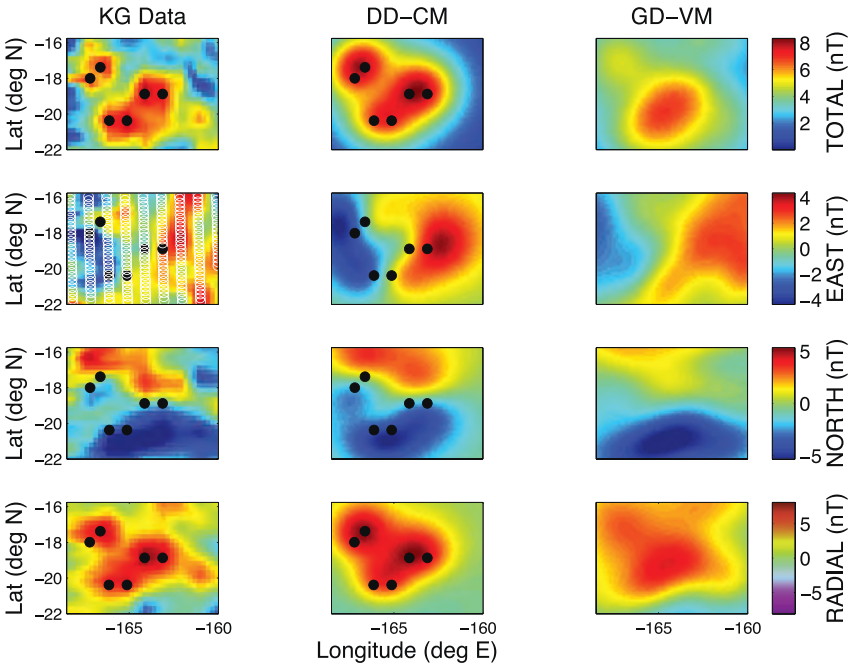

Fig. 12. Area 5 best-fit results with both inversion algorithms. Figure details are as in Fig. 8, except that magnetometer measurements are taken from K-MAG, 2009 day 123, altitude 33.3 km.

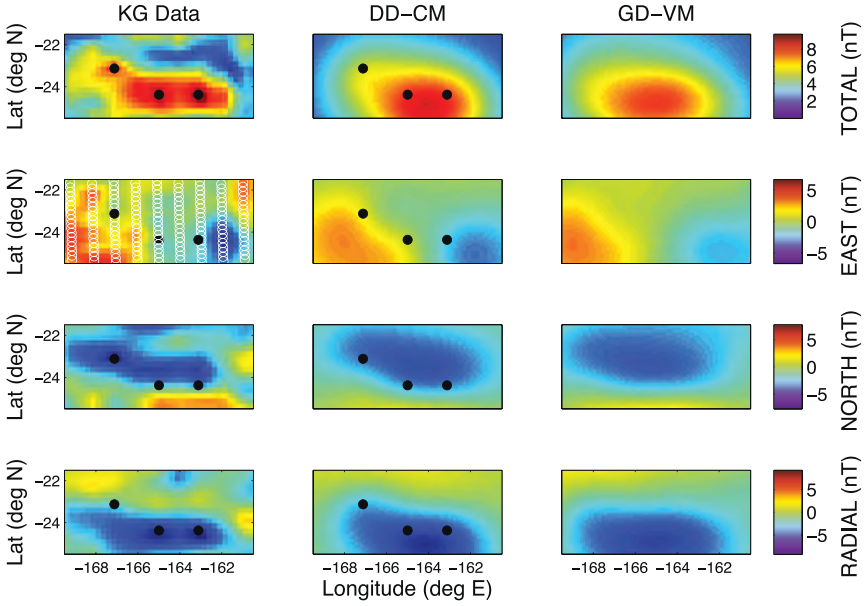

Fig. 13. Area 6 best-fit results from both inversion algorithms. Figure details are as in Fig. 8, except that magnetometer measurements are taken from K-MAG, 2009 day 123, altitude 32.4 km.

area 2, and its source body characteristics; we will investigate, for example, oppositely magnetized blocks of magnetization in this region (cf. Parker, 1988).

For area 8, the large error arises from the flatness of the error space, instead of the existence of multiple minima (Fig. 18). In particular, the declination of this nearly equator-pointing magnetization vector is poorly constrained, with results spanning a range of ∼100° of arc (a result found to be true using either the DD-CM or GD-VM algorithm). Again, without the error maps provided by the DD-CM algorithm, we would not have been able to isolate and understand these different sources of uncertainty in areas 2 and 8.

Next, we calculate the mean magnetization strength for all study areas using the best-fit depths and magnetic moments recovered by both the DD-CM and GD-VM algorithms (Table 1). For this calculation, the area of the magnetic anomalies is taken as the area across which the magnetic field $B \geq B_{max}/4$, where B_{max} is the peak magnetic field in a given study area. We choose to approximate the thickness of the magnetic material as twice the average of the best-fit magnetic source depths. Most values cluster in the 0.1–0.3 A/m range found by Purucker et al. (2012), who studied a region similar to area 1. A few isolated datasets at the lowest altitudes show higher magnetizations, but with the exception of area 9, average magnetizations for a particular study area across all

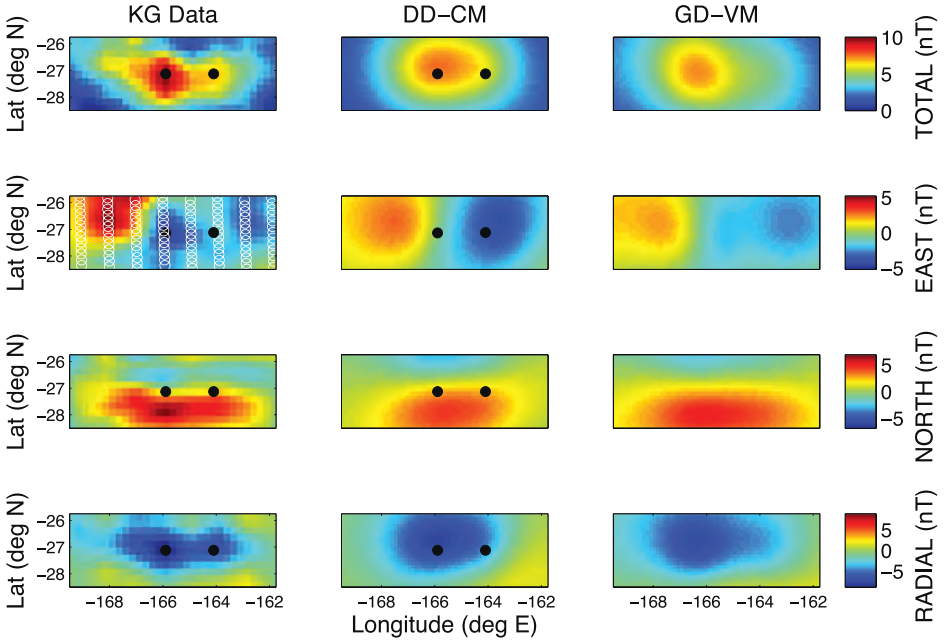

Fig. 14. Area 7 best-fit results from both inversion algorithms. Figure details are as in Fig. 8, except that magnetometer measurements are taken from K-MAG, 2009 day 123, altitude 31.7 km.

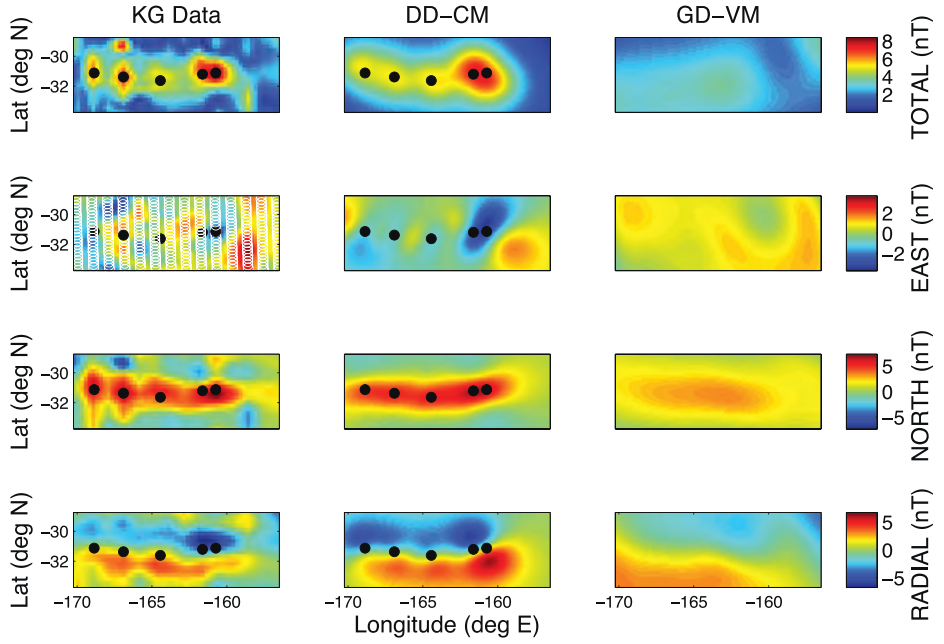

Fig. 15. Area 8 best-fit results from both inversion algorithms. Figure details are as in Fig. 8, except that magnetometer measurements are taken from K-MAG, 2009 day 123, altitude 31.4 km.

datasets are close to the 0.1–0.4 A/m range suggested by Wieczorek and Weiss (2010) for mare basalts and mafic impact melt breccias. Even for area 9, only the GD-VM average magnetization is outside this range.

In most cases the GD-VM algorithm returns higher values for magnetizations than the DD-CM algorithm. This is a result of the shallower depths returned by the GD-VM algorithm, which arise because of the sheet-like nature of the magnetic source, compared to the dipolar model in the DD-CM algorithm. In general the depth of the magnetic source bodies is not well constrained from our results, due to the possibility of non-uniquely trading depth with moment.

Finally, best-fit paleopoles for all datasets are calculated from the best-fit magnetization directions (Butler, 1998) (Fig. 21, Table 3). The uncertainties derived from the methods described in the Methods section yield a circular error ellipse for each area that becomes distorted when its paleopole is calculated. Hence we calculate the two different semi-axes of the ellipse along the great circle path from the site to pole (*dp*) and the semi-axes of the ellipse perpendicular to that path (*dm*) (Butler, 1998). For area 2, we also show the paleopoles from the two local error minima found in the DD-CM method, particularly because one falls very close to the paleopole for area 1 (within its uncertainty), while the other paleopoles from areas 3 and 6 (within the uncertainty of 6).

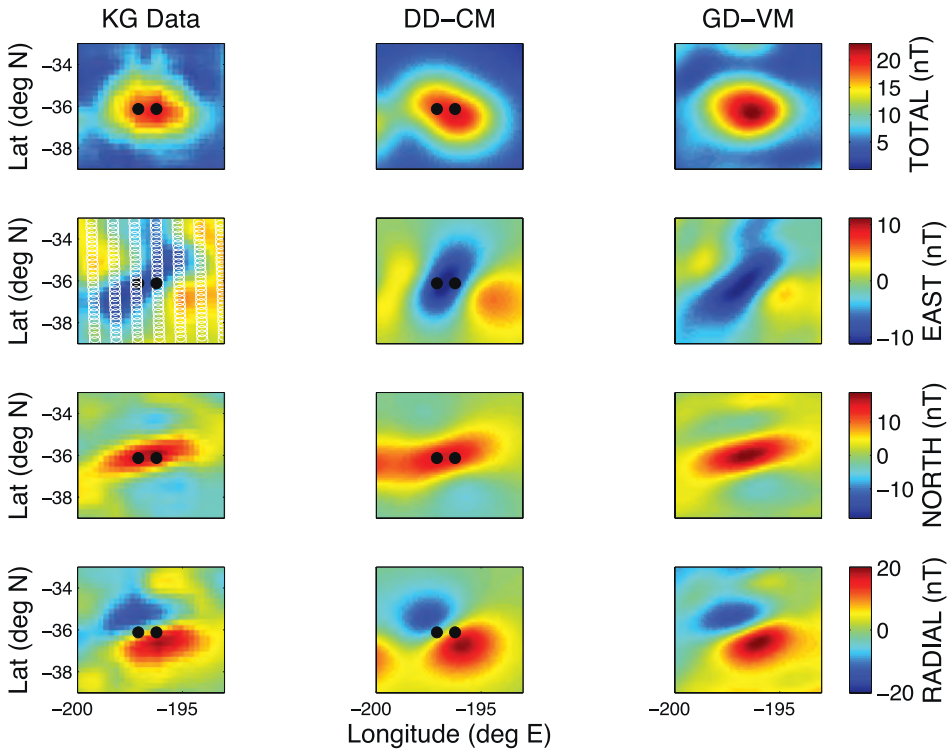

Fig. 16. Area 9 best-fit results from both inversion algorithms. Figure details are as in Fig. 8, except that magnetometer measurements are taken from K-MAG, 2009 day 123, altitude 28.3 km.

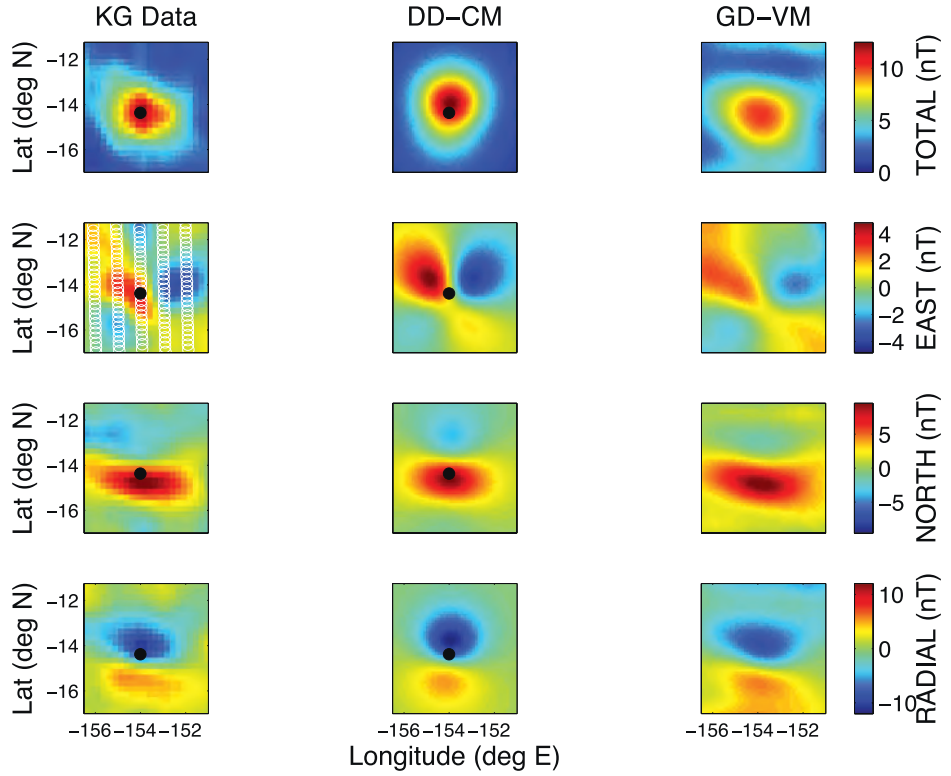

Fig. 17. Area 10 best-fit results from both inversion algorithms. Figure details are as in Fig. 8, except that magnetometer measurements are taken from K-MAG, 2009 day 123, altitude 34.2 km.

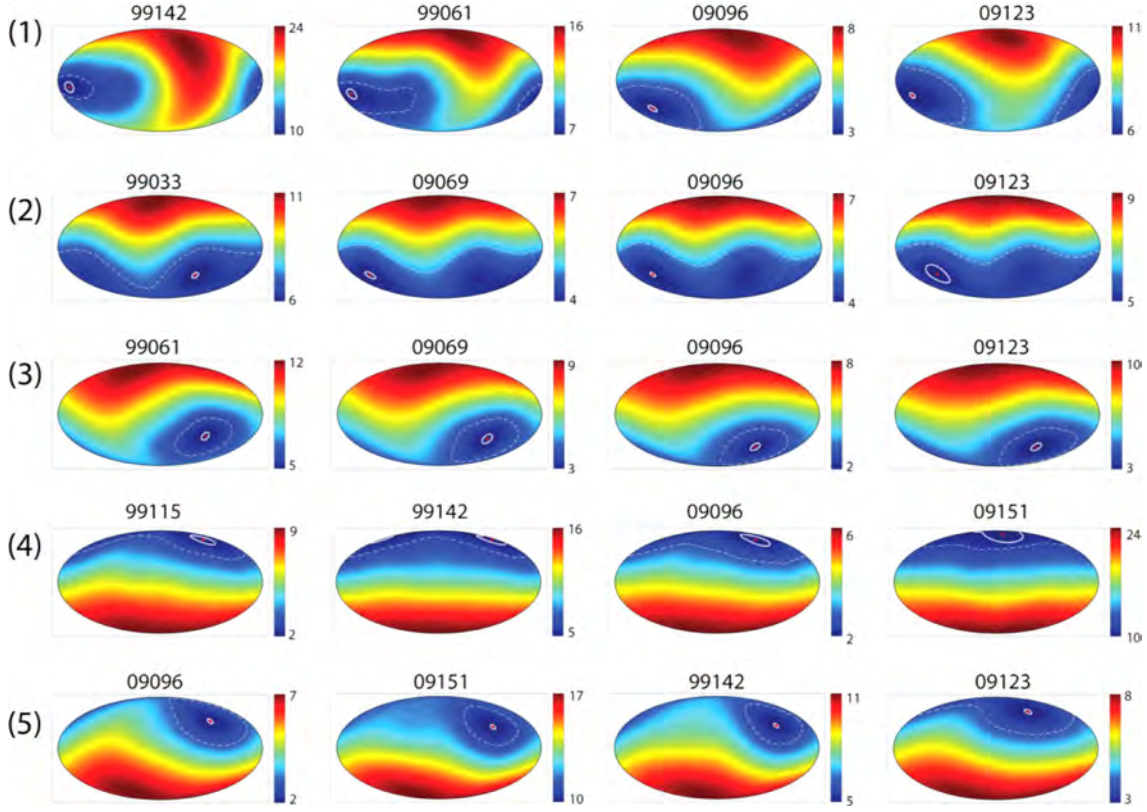

Fig. 18. RMS error map (nT) for the magnetization direction for all datasets for SPA study areas 1–5, obtained using the DD-CM algorithm. Southern hemisphere is positive inclination; the whole-sphere Mollweide projection is centered at 0° inclination and 0° declination. The solid white contour indicates one angular standard deviation of dispersion from the best-fit solution (red dots, Table 1), from Monte Carlo simulations of the addition of 1 nT Gaussian noise to observations, using the DD-CM algorithm. The larger, dashed white contour indicates the minimum error solution plus 1 nT, a measure of uncertainty using an arbitrary threshold equal to the measurement uncertainty (not used in our final analysis). The error from Monte Carlo simulations of the effects of displacing the nominal source dipole locations by 0.5° is not shown, and nor is the 95% confidence interval from averaging different altitude data sets. (For interpretation of the references to colour in this figure legend, the reader is referred to the web version of this article.)

3.2. Comparison with other magnetic paleopoles

In Fig. 22b-d we show paleopoles from isolated magnetic anomalies studied by Takahashi et al. (2014) and Arkani-Hamed and Boutin (2014), as well as paleopoles inferred from the magnetization of the crust at craters (Arkani-Hamed and Boutin, 2014). The magnetized crust paleopoles from Arkani-Hamed and Boutin (2014) are the means of the values listed in their Table 2. None of the anomalies studied by these groups were inside SPA. To compare our results with these three datasets, we reverse all of our paleopoles into the same southern hemisphere (Fig. 22a), as in Takahashi et al. (2014). Here we have dropped the paleopole found from the mean of all data sets at area 2, and only show the paleopoles from the two local error minima in the DD-CM algorithm.

Takahashi et al. (2014) found paleopoles that cluster into two groups, one near the present pole, and another at mid-latitudes. We find a wider dispersion in the distribution of our paleopoles, but we do find some clustering at the present pole (areas 5, 7 and 10), as well as some near their mid-latitude cluster (areas 3, 6, and 8). The remaining poles are not easily assigned to either of these clusters. However, overall, the paleopoles we find do seem to avoid longitudes on the farside (the bottom half of the sphere in Fig. 22a), and latitudes $< 30°$. None of the paleopoles from Arkani-Hamed and Boutin (2014) show obvious correlation with any of the clustering found here or in Takahashi et al. (2014).

Finally, we note that many of the paleopoles are substantially separated by their error ellipses, such that it is unlikely that only one or two paleopoles could be used to explain all of the anomalies, without severely affecting their RMS error values. This can also be visualized by examining the error spaces in Figs. 18 and 19; because most anomalies are at similar latitudes and longitudes (most within ~30°), the diversity in paleopole locations is mostly determined by the diversity in magnetization directions. Hence, the diversity in RMS error minima in Figs. 18/19 also graphically illustrates the diversity in paleopole locations.

In the next section, we address possible origins for the dispersion seen in our study, and test some of the hypotheses for anomaly formation.

4. Discussion

The wide variation in magnetic paleopoles derived from SPA's magnetic anomalies presents a puzzle. In Sections 4.1–4.4, we discuss the implications of the diverse paleopole locations for the formation of these anomalies, the history of true polar wander, and the nature of the lunar dynamo.

4.1. Magnetization by impact processes

A long-standing hypothesis is that the strongest lunar magnetic anomalies are genetically related to the antipodes of the Imbrium, Orientale, Serenitatis and Crisium basins (Hood and Williams, 1989; Hood et al., 2001; Lin et al., 1998). Compression and amplification of the IMF by impact-produced plasma may be strongest at the basin antipode, where impact ejecta may also preferentially

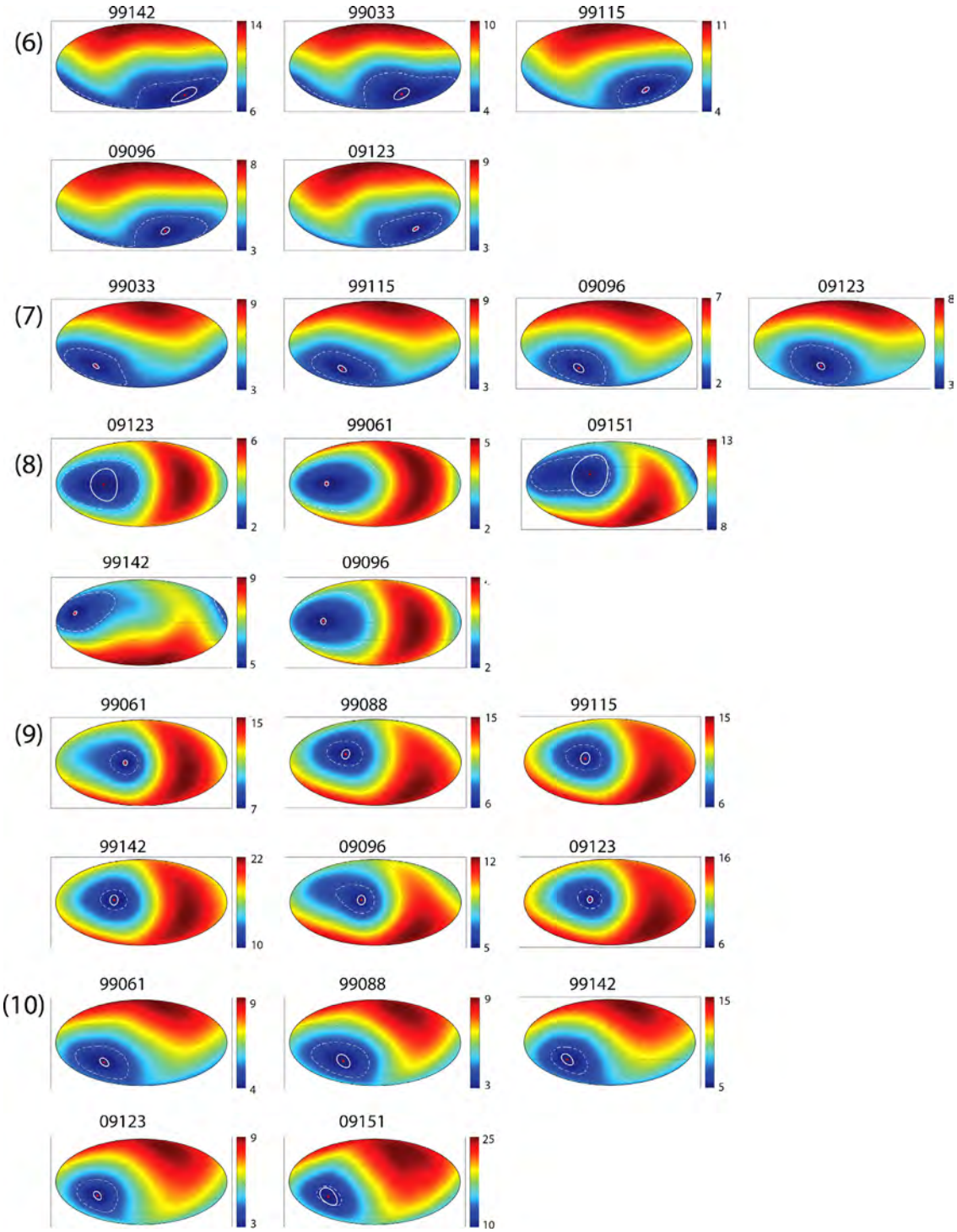

Fig. 19. RMS error map (nT) for the magnetization direction for all datasets for SPA study areas 6–10, obtained using the DD-CM algorithm. Description is as in Fig. 18.

collect (Hood and Artemieva, 2008). The antipodes of the Imbrium and Serenitatis basins are close to our study areas (Fig. 1), suggesting this process may be responsible for forming the anomalies we have examined here. If true, antipodal ejecta may become magnetized via either thermo-remanent magnetization (TRM) or shock-remanent magnetization (SRM). Below we assess these two possibilities.

4.1.1. TRM in an impact-produced field

If the magnetization were produced by a TRM, hot ejecta would cool in the presence of transient IMF-amplified fields that would last, at most, for one day. Assuming a thermal diffusivity of 10^{-6} m^2/s, the thermal cooling timescale for one day is $<$1 m. Therefore, TRM would be restricted to $<$1 m of material. The magnetic moments we find across all SPA study areas range between 10^{13} Am^2 and 10^{14} Am^2. Using source body horizontal extents from Fig. 1 (black dashed boxes), depths of $\sim$1 m lead to high TRM magnetizations ranging between 10^3 and 10^4 A/m. These values are 3–4 orders of magnitude higher than samples recovered by Apollo missions. Additionally, the top $\sim$1 m would have been completely overturned and demagnetized in the time since the antipodal impact $\sim$4 billion years ago (Arnold, 1975). Therefore, TRM from

impact-related fields is implausible, in agreement with Hood and Artemieva (2008).

4.1.2. SRM in an impact-produced field

Alternately, impact shock pressures from the deposition of ejecta at the antipode may create SRM in the ejecta deposit. However, to allow unidirectional SRM to be stably imparted to a large-scale (e.g. $>4000\,km^2$ for areas 1 and 2; $>30{,}000\,km^2$ for areas 5–8) geologic formation, the shock waves must pass through the rock when the entire region is at rest. Shock waves begin propagating through the rock instantly upon impact, yet at that moment the ejecta is still traveling at 2.0–2.4 km/s (Hood and Artemieva, 2008). Therefore, the ejecta at the antipode will change orientation as it comes to rest, after any SRM has formed, such that the total remanence of the ejecta deposit will be randomized and nulled. Hood and Artemieva (2008) also rule out SRM in the ejecta, using a different line of reasoning.

It is possible that the underlying rock could be shocked by the impacting ejecta and acquire a unidirectional SRM (Hood and Artemieva, 2008). However, we suggest that there are two problems with this hypothesis. Firstly, one would expect nearly vertical local magnetization if the SRM producing field was compressed by solar wind plasma (see, for example, field lines in Figs. 8–9 of Hood and Artemieva, 2008). Instead, only one magnetic anomaly, area 4, has a nearly vertical magnetization, and the rest show a preference for low inclinations, if anything (the rest are at least $>33°$ away from the vertical, Fig. 20).

Secondly, deposition of impact ejecta would take place over a short period of time, over which the ambient field direction is likely to be nearly constant. There are only two basin antipodes within SPA, which implies that the magnetic anomalies should have one of two magnetization directions. Roughly, areas 1–3 (northwest cluster), 4, and 9 are antipodal to Imbrium, while areas 5–8 (eastern stripes), and 10 are antipodal to Serenitatis. First, we consider the five anomalies at the Imbrium antipode. Here we find that areas 1 and 3 have magnetization vectors 109° apart (Fig. 21). The magnetization at area 4 is 95° from that at area 1 and 70° from area 3. The magnetization at area 9 (Mare Ingenii) is 104° from area 1, 140° from area 3, and 128° from area 4. All of these separations are well outside the error ellipses. The only two clusters are the directions of areas 1 and 2, and possibly area 3 with the second error minimum obtained at area 2. In sum, there are at least four widely separated magnetization directions near the Imbrium antipode, all well separated by their error ellipses. It is plausible the similar directions at areas 1 and 2 suggest this pair was magnetized by deposition of impact ejecta, but it would not explain the magnetization of the other areas.

At the five anomalies near the Serenitatis antipode, areas 7, 8, and 10 have similar directions, but 5 and 6 are well separated from each other and from 7, 8, and 10 (Fig. 21). Therefore, we conclude again that it is not likely that the Serenitatis impact is responsible for magnetizing all of these anomalies.

In sum, the diversity of directions argues against the SRM hypothesis, or at least allows only a subset of the geographically clustered anomalies to be due to SRM. Similar arguments can be applied to ruling out SRM from surface seismic waves. Considering all of the observations above, we conclude that at least some of the magnetic source bodies in SPA were magnetized in a lunar dynamo field, rather than a field associated with impact events.

4.2. Magnetized South Pole-Aitken basin ejecta or volcanic bodies?

Wieczorek et al. (2012) proposed that material from the SPA impactor might be the source of many of the SPA basin's magnetic anomalies, and even other anomalies across the Moon. Under this hypothesis, hot iron-enriched material from the SPA impactor acquired a TRM in a dynamo field. However, if SPA ejecta landed hot and cooled in a dynamo field, the resulting anomalies should all have the same magnetization direction (but see Section 4.3.4). Instead, the diverse magnetization directions (see Section 4.1.2, above) suggest that they were magnetized at different epochs.

The last remaining viable hypothesis is that magnetic anomalies in the northern SPA basin formed as a result of magnetized sub-surface dikes (Purucker et al., 2012). Dikes forming over long time periods would permit different magnetization directions during different magnetic epochs. The cluster of three paleopoles close to the present pole (areas 5, 7 and 10, Fig. 22a) would suggest a traditional axial-aligned dynamo magnetized these dikes when the Moon was in its present orientation. However, the diversity in paleopoles seen is still enigmatic (see Section 4.3). Further, if the dike hypothesis is true, this implies that the dikes near SPA are special in some way, since the nearside of the Moon, covered much more extensively by volcanism (and presumably associated with subsurface dikes), shows no magnetic structures like those at SPA. Andrews-Hanna et al. (2014) reported linear gravity-gradient anomalies that may be dikes, but so far, no obvious correlation between these structures and magnetic anomalies have been found. We note that Gong and Wieczorek (2016) find a correlation between magnetization and gravity anomalies in some locations.

4.3. Possible explanations for diverse magnetic field directions

The above arguments suggest the magnetizing fields for many of the SPA anomalies arose from a dynamo. However, they do not offer an obvious explanation for the diversity in field directions. Due to the small size of the lunar core, and the rapid decay of magnetic quadrupole and higher terms as a function of distance, it is likely that the ancient lunar dynamo was dominantly dipolar at the surface (Weiss and Tikoo, 2014). If the dipole was aligned with the Moon's spin axis, the magnetization directions contain information about the Moon's paleopole. The diverse paleopoles in Fig. 21 seem to imply large amounts of true polar wander (Goldreich and Toomre, 1969; Runcorn, 1983). While the diversity in Fig. 21 is surprising, in comparison with the results of (Arkani-Hamed and Boutin, 2014; Takahashi et al., 2014) (Fig. 22a), the diversity of paleopoles seen in our findings is still greater. Below we consider some possible explanations for the diverse paleopole locations.

4.3.1. Non-axially aligned dipoles and impact-induced dynamos

Currently, our understanding of the nature of the lunar dynamo is limited. Paleomagnetic studies favor a dynamo that existed from approximately 4.2–3.3 Ga ago. Mechanisms for sustaining such a long-lived core dynamo are uncertain, with recent proposals for dynamos driven by mechanical stirring from impacts and precession (Dwyer et al., 2011; Le Bars et al., 2011; Weiss and Tikoo, 2014). However, it is not known if these dynamos produce the same field organization as the Earth's dynamo. It may be possible that these exotic dynamos exhibit more variable dipole axis directions, which could explain the diversity of paleopoles seen. Unfortunately, more work modeling small dynamos like that of the Moon is needed before evaluating this hypothesis further.

4.3.2. Secular variation

Another possible origin for the diverse paleopole locations is geomagnetic secular variation of a dynamo that is on average aligned with the lunar spin axis. The Earth's spin axis is presently 11° away from its magnetic dipole axis, and it is plausible that the Moon's ancient dipole axis was also not exactly aligned with its spin axis. It is also possible that secular drift might be larger on a body with a small core such as the Moon. However, some of the

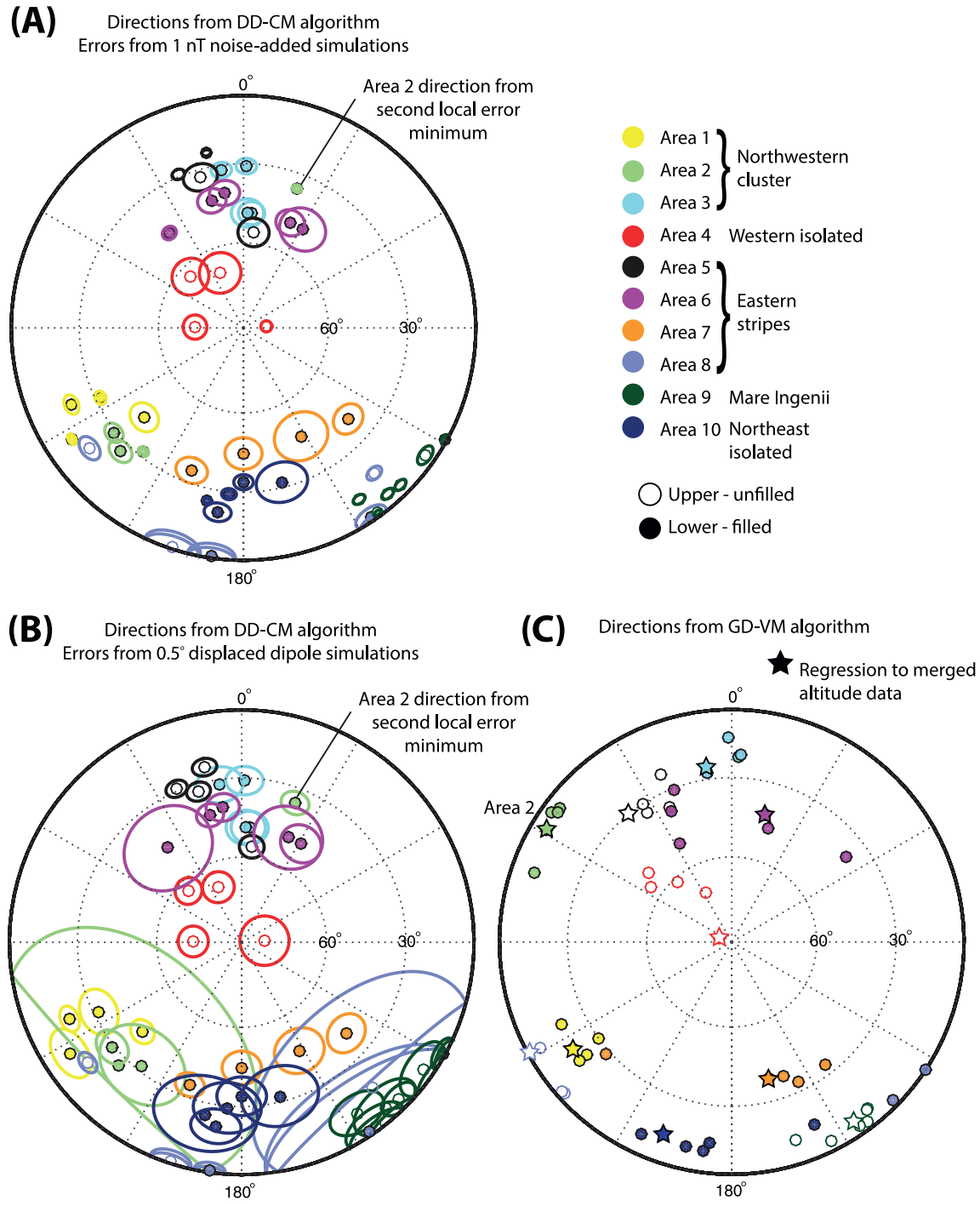

Fig. 20. Best-fit magnetization directions for study areas defined in Fig. 1, for all datasets in Figs. 2 and 3. Directions derived from different altitudes and different spacecraft at the same study area are represented by the same color. Positive inclinations are in the lower hemisphere (filled circles). (A & B) Results for the DD-CM algorithm. Ellipses in A represent one angular standard deviation of dispersion from 1 nT noise simulations. Ellipses in B represent one angular standard deviation of dispersion from simulations of source dipoles displaced from their nominal positions (0.5°), (C) Results from the GD-VM algorithm, including results from regressions to merged data at all altitudes shown in Fig. 2 and Fig. 3, within a given study area (stars).

paleopole locations at SPA are over ~75° apart (after accounting for the possibility of reversals, Fig. 22a), and over the timescale of magnetic anomaly formation, the mean dipole orientation might average to be aligned with the spin axis. Presently, we have little information available about the lunar dynamo to further evaluate the role of secular variation in explaining the diversity of paleopole directions.

4.3.3. True polar wander over long timescales

The large amount of polar wander implied by the paleopoles is difficult to reconcile with other geophysical constraints for the orientation history of the Moon. Currently there are two comprehensive studies that derive estimates of the degree of polar wander on the Moon due to long-term changes in the Moon's moments of inertia (Garrick-Bethell, 2016). The first uses the shape

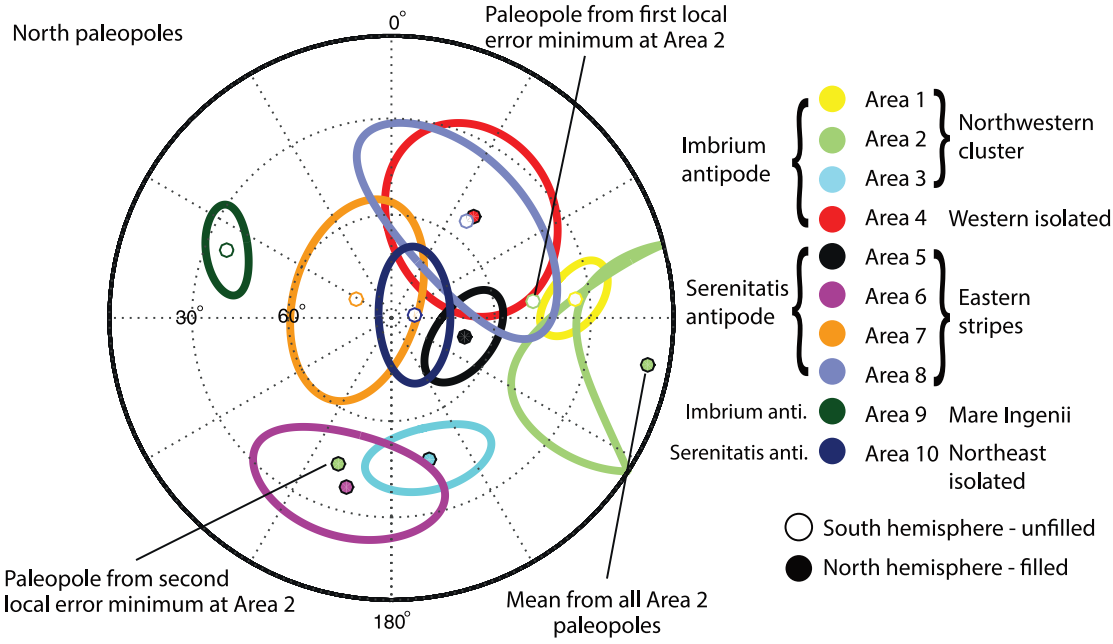

Fig. 21. SPA magnetic paleopoles. Paleopoles are the mean of the combined results from the DD-CM and GD-VM algorithms, from all directions (altitudes) shown in Fig. 20. Ellipses represent the 95% confidence interval obtained when calculating the mean direction from the combined DD-CM and GD-VM results, plus the dispersion from Monte Carlo simulations of time-dependent fields and dipoles displaced from their nominal locations (see Methods). Error ellipses are not calculated for the two different minimum error solutions for area 2 from the DD-CM algorithm.

and gravity of the Moon exterior to large basins to establish the earliest orientation of the Moon (Garrick-Bethell et al., 2014). The authors find the present lunar pole has changed by ~36° from its earliest axis, but it does not coincide with any of the paleopole clusters we find (Fig. 22a). The second study uses polar hydrogen deposits as a constraint on the history of polar wander, and infers that up to ~10° of paleolatitude change has occurred (Siegler et al., 2016). However, they cannot readily produce the large paleopole changes implied by the anomalies studied here. In summary, the limited number of available geophysical models that estimate lunar polar wander cannot produce the diversity and large magnitude of paleopole changes required to explain our observations. Interestingly, we find that all of our paleopoles are > 35° from the present equator (Fig. 22a, accounting for reversals), which may be due to the difficulty in producing the large required changes in the Moon's moments of inertia.

4.3.4. True polar wander due to SPA formation

Very large initial changes in the Moon's moments of inertia due to SPA's crater might have produced large amounts of polar wander. Eventually, these changes must have subsided over millions to billions of years, since the gravity signature observed today is muted (Zuber et al., 2013). If hot material was cooling in the presence of a dynamo field throughout the Moon's reorientation, its magnetization could in principle capture multiple lunar orientations, thereby producing the diversity of paleopole locations. Some of this hot material could be iron-rich material from the SPA impactor (Wieczorek et al., 2012). Following impact, the free precession damping time of the Moon is $\sim 2 \times 10^5$ years (Peale, 1976; Williams et al., 2001), assuming a semimajor axis of 30 Earth radii, dissipation quality factor $Q = 50$ and degree-2 love number $k_2 = 0.1$ (which we assume to be representative of the Moon when SPA formed). The length scale for cooling in $\sim 2 \times 10^5$ years is ~3 km (assuming a thermal diffusivity of 10^{-6} m^2 s^{-1}), which is small compared to the scale of the anomalies we observe, but perhaps not so much as to preclude recording a measurable magnetization.

However, using a simple model for reorientation, we find that density anomalies produced by SPA's crater do not produce paleopoles that overlap with those of its magnetic anomalies. In our model, we replace SPA's gravity potential inside the outer topography rim with values between −3 times the maximum, and +2 times the maximum of the present day potential, in increments of 0.25 times the maximum potential. The inertia tensor and paleopoles were then calculated for each of these cases using the resulting globally calculated degree-2 spherical harmonics (cf. Garrick-Bethell et al., 2014). These positive and negative gravity values represent very different models of SPA's effects, but illustrate the range of paleopoles that are possible. We find the maximum extent of true polar wander from SPA's formation passes close to the paleopoles from areas 7 and 10 (Fig. 22a, the negative anomaly path approaches the center of SPA as the anomaly size grows, as expected). However, these anomalies are already close to the present pole, and do not need to be explained by polar wander. We do find that the limits of polar wander approach areas 4 and 8, such that this process could plausibly explain some of these magnetic paleopoles. Unfortunately, the paleopoles from areas 1, 2, 3, 5, and 9, and to a lesser extent area 6, do not come close to the paleopoles produced by SPA. Thus, cooling of SPA ejecta deposits over short timescales (~10^5 years), or even dikes that formed when the Moon resided at any of the SPA-produced paleopoles, cannot fully explain the observed diversity of magnetic paleopoles we find.

There are many unknowns in modeling the paleopoles allowed by SPA's formation. For example, reorientation and magnetic anomaly formation depends on the SPA impact's effect on dynamo operation (Arkani-Hamed and Olson, 2010a, 2010b), the inertia tensor of the Moon just before SPA formation and the length scale (and thereby cooling timescale) of the materials making up the anomalies. Furthermore, the spin vector of the Moon will be freely precessing around its angular momentum vector during the free precession damping timescale. If the dynamo after SPA impact retained its alignment along the Moon's angular momentum vector, this precession could broaden the range of paleopoles permitted (essentially accessing a range of paleopoles around the pale-

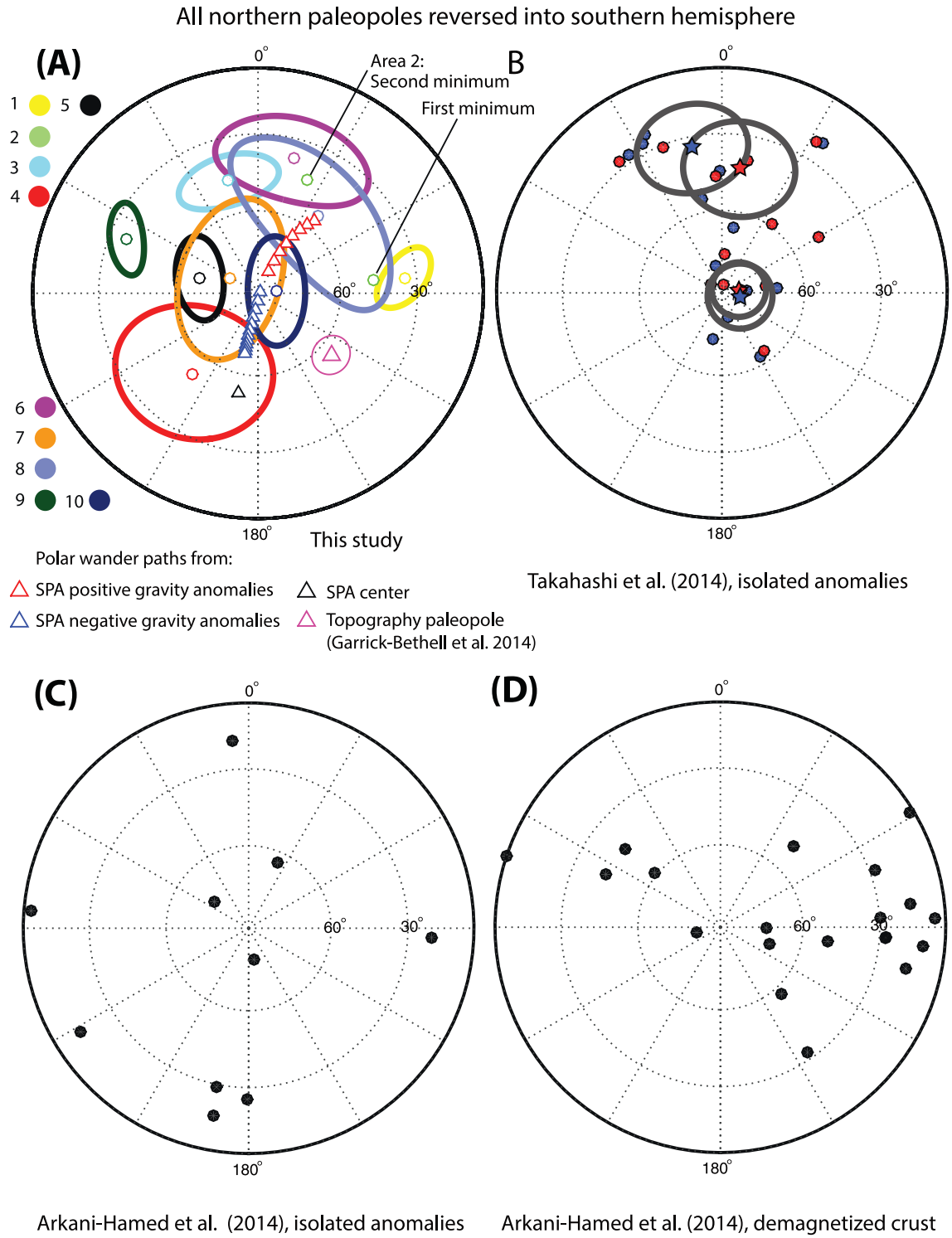

Fig. 22. Paleopoles from SPA anomalies compared with published paleopoles from other anomalies. All figures show the southern hemisphere (all points are southern latitudes). (A) Our results from Fig. 21, with all north poles reversed into the southern hemisphere. The paleopole obtained from the mean of all data at area 2 (see Fig. 21) has been omitted in this figure. Red and blue triangles are possible lunar paleopoles resulting from SPA's gravity anomaly immediately after its formation, assuming an extreme range of density anomaly models; red (blue) points are positive (negative) density anomalies (see Section 4.3.4). SPA's center (a limiting paleopole for very negative density models of SPA) is shown at (−53.2° S, 191° E) (black triangle). The magenta triangle shows the paleopole dervied from the tidal component of the Moon's topography, outside of large basins (Garrick-Bethell et al., 2014). (B) Paleopoles from the 11 anomalies reported by Takahashi et al. (2014). No anomalies are within SPA. Blue (red) points represent inversions from Kaguya (Lunar Prospector) data. In many cases, multiple points represent paleopoles from single sites. Stars represent the means of the two clusters. (C) Paleopoles from 10 isolated magnetic anomalies reported by Arkani-Hamed et al. (2014). (D) Paleopoles from crustal magnetization at 20 impact craters reported by Arkani-Hamed et al. (2014). (For interpretation of the references to color in this figure legend, the reader is referred to the web version of this article.)

opoles shown in Fig. 22a, with the range depending on the precession angle). Therefore, we cannot definitively rule out polar wander processes as the origin for some of the diverse paleopole locations at SPA.

A variant of the hypothesis of iron-rich SPA ejecta (Wieczorek et al., 2012) is the cooling of iron-rich "sesquinary" (Zahnle et al., 2008) impactors formed by the SPA impact. Ejected into orbit immediately after impact, studies on various planetary bodies show that these impactors can return to a body from 10^4 years (Nayak et al., 2016) to 10^6 years (Gladman et al., 1995) post-impact, at approximately escape velocity (Nayak and Asphaug, 2016). With reimpacts spread across this timescale, reaccreting iron-rich material originally from SPA, either still hot from the impact or heating upon re-impact, could record a diverse set of orientations as the Moon reorients in response to moment of inertia changes. Across this timescale, impact locations become random; such sesquinary magnetism caused by these iron-rich impactors would be widely distributed around the Moon.

5. Conclusions

Using two different inversion methods, we find diverse directions of magnetization among magnetic anomalies in the northern SPA basin. The diverse directions help rule out impact-related fields as their only origin. Intrusive bodies, such as the dikes proposed by (Purucker et al., 2012), are a plausible explanation. The diverse paleopole locations could imply large amounts of true polar wander, but true polar wander inferred independently from gravity (Garrick-Bethell et al., 2014) and hydrogen deposits (Siegler et al., 2016) implies more modest changes in the Moon's orientation. The diverse directions argue against the hypothesis that they all formed from iron-rich SPA ejecta that cooled in a dynamo field (Wieczorek et al., 2012). A simple gravity anomaly model for large amounts of SPA-produced reorientation fails to explain at least five of the paleopoles observed, but many unknowns remain in modeling this process. Some SPA ejecta may have produced iron-rich sesquinary impactors that landed across the Moon and recorded orientation changes as they cooled in a dynamo field. A dynamo that was not aligned with the lunar spin axis remains a plausible explanation for all observations, but gaps remain in our ability confirm this hypothesis. The wide variety of viable hypotheses and large number of unknowns highlight the complexity of interpreting the origins of lunar magnetic anomalies and their paleopoles.

Acknowledgments

This research was supported by the NASA Discovery Data Analysis Program (grant NNX16AJ07G), and the BK21 plus program through the National Research Foundation (NRF), funded by the Ministry of Education of Korea. MN acknowledges support from the National Defense Science and Engineering Graduate (NDSEG) Fellowship, 32 CFR 168a, funded by the Air Force Office of Scientific Research, Department of Defense. Partial support was also provided by *(1)* The Alfred P. Sloan Foundation, *(2)* The UC Santa Cruz / NASA Ames University Affiliated Research Center, Aligned Research Program and *(3)* Red Sky Research, LLC. Thanks to Rob Coe and Gary Glatzmaier for helpful comments. Opinions, interpretations and recommendations expressed are those of the authors and are not necessarily endorsed by the US Air Force or the Department of Defense.

Appendix A. Comparison of magnetic field observations with best-fit models for all datasets

We use 45 datasets for the analysis in this work, the total field plots of which are shown in Fig. 2 (areas 1–5) and Fig. 3 (areas 6–10). In Figs. 8–17 we presented example magnetic field maps for the best-fit source magnetizations, from both inversion algorithms, for areas 1–10, respectively. Here we present the magnetic field maps for the best-fit source magnetizations for the 35 remaining datasets.

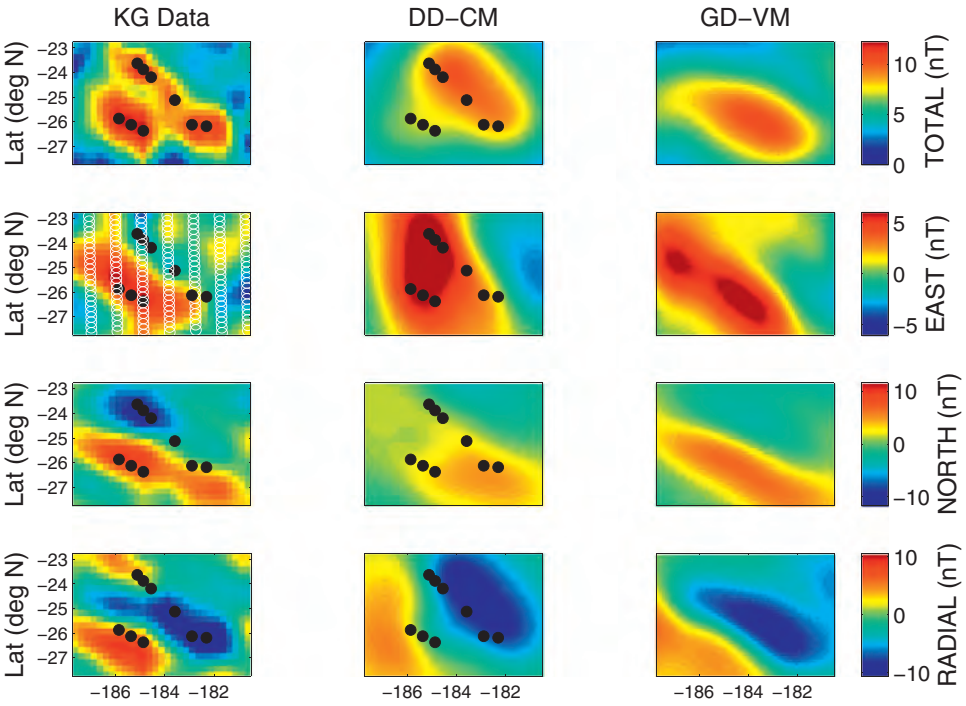

Fig. A1. Area 1 best-fit results for both inversion algorithms. (Left column) K-MAG observations in the lunar wake on 2009 day 123, compared to (Middle column) a model with manually placed dipoles of equal magnetization (DD-CM) and (Right column) a grid-based model with variable magnetizations (GD-VM). Source dipoles in the DD-CM algorithm are approximately located at maxima of the observed total field (black dots). White dots in the east panel are locations of spacecraft magnetometer measurements. The mean measurement altitude is 31.6 km. Longitude (degrees east) is indicated on the x-axis.

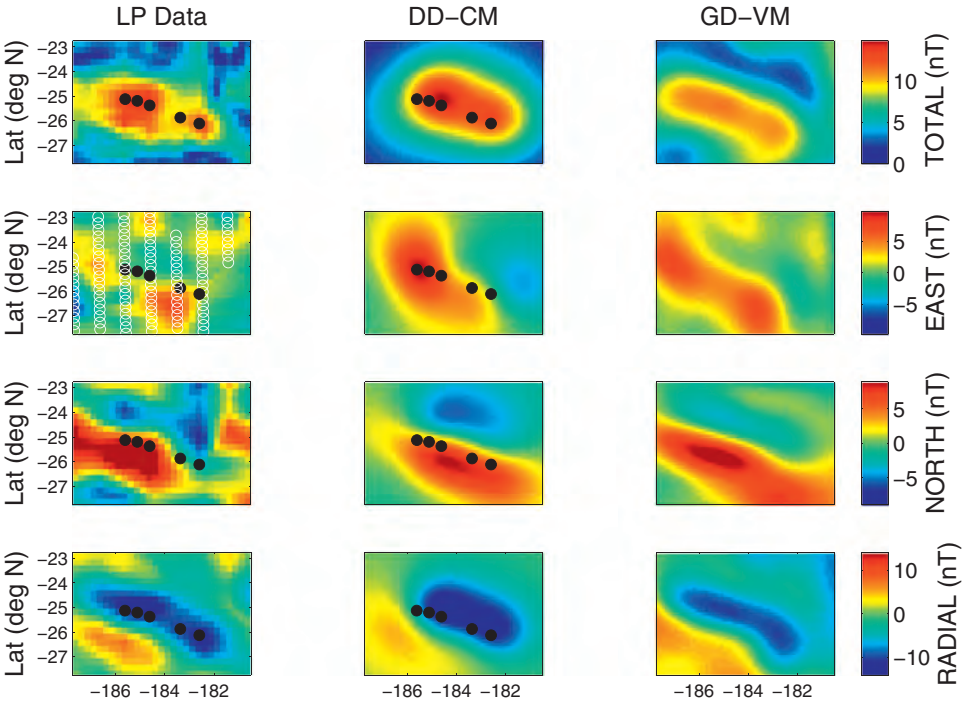

Fig. A2. Area 1 best-fit results for both inversion algorithms. Details are as in Fig. A1, except that the mean measurement altitude is 31.1 km and the observations are from 1999 day 61.

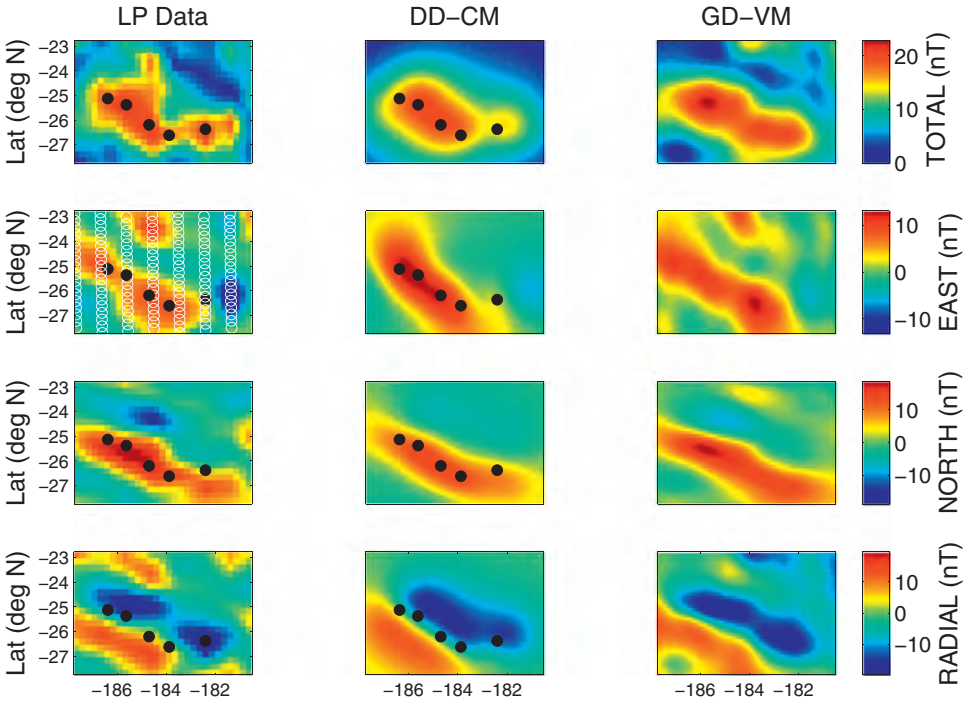

Fig. A3. Area 1 best-fit results for both inversion algorithms. Details are as in Fig. A1, except that the mean measurement altitude is 21.4 km and the observations are from 1999 day 142.

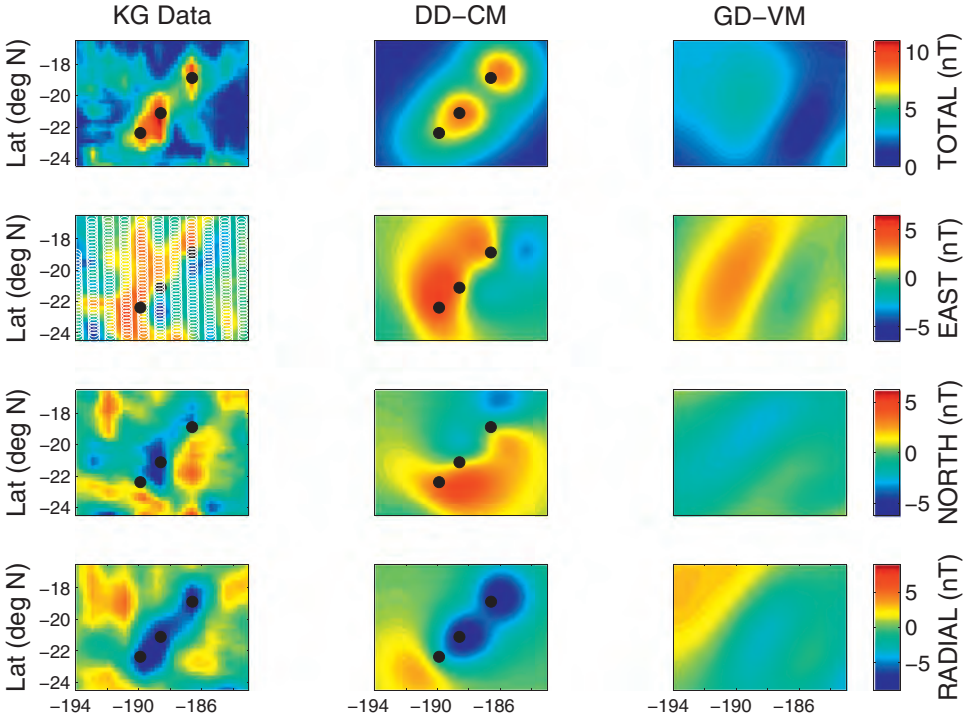

Fig. A4. Area 2 best-fit results for both inversion algorithms. Details are as in Fig. A1, except that the mean measurement altitude is 43.5 km and the observations are from 2009 day 69.

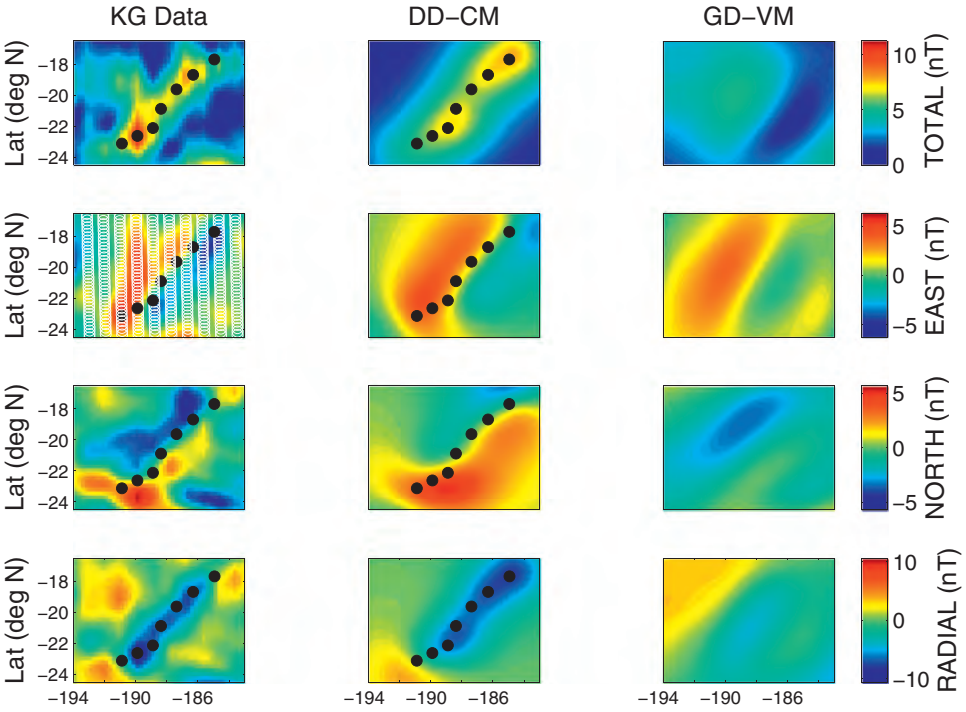

Fig. A5. Area 2 best-fit results for both inversion algorithms. Details are as in Fig. A1, except that the mean measurement altitude is 38.5 km and the observations are from 2009 day 96.

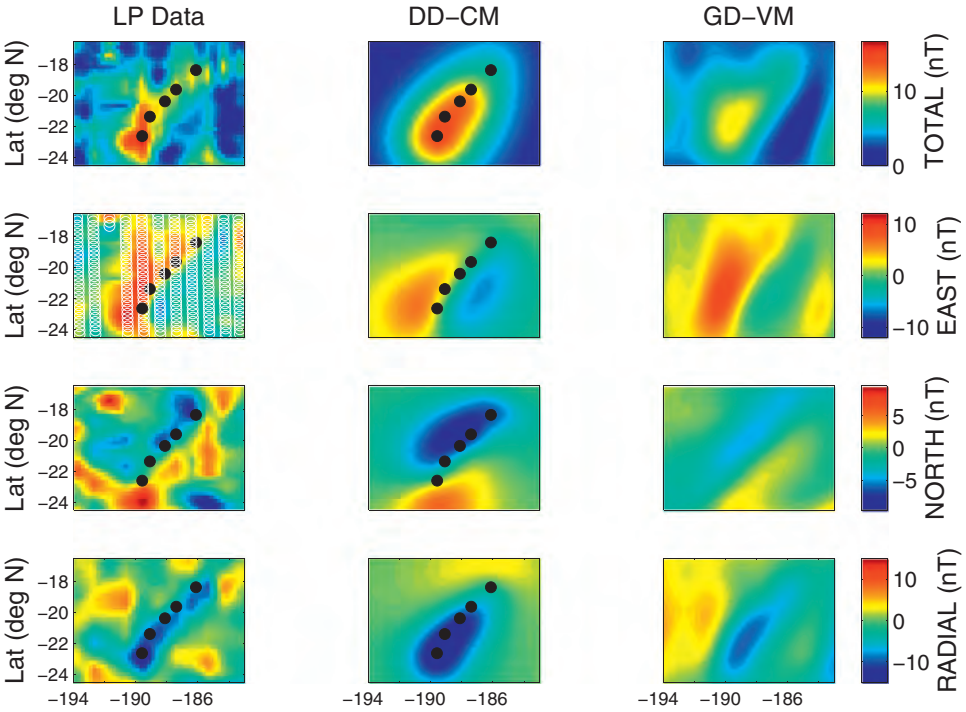

Fig. A6. Area 2 best-fit results for both inversion algorithms. Details are as in Fig. A1, except that the mean measurement altitude is 31.1 km and the observations are from 1999 day 33.

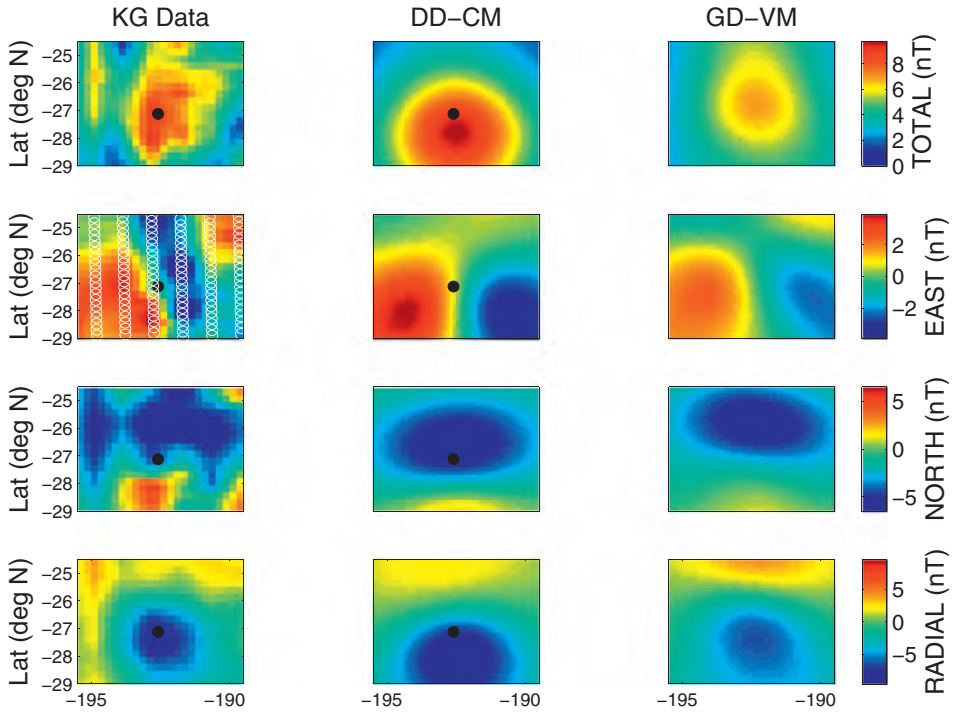

Fig. A7. Area 3 best-fit results for both inversion algorithms. Details are as in Fig. A1, except that the mean measurement altitude is 42.8 km and the observations are from 2009 day 69.

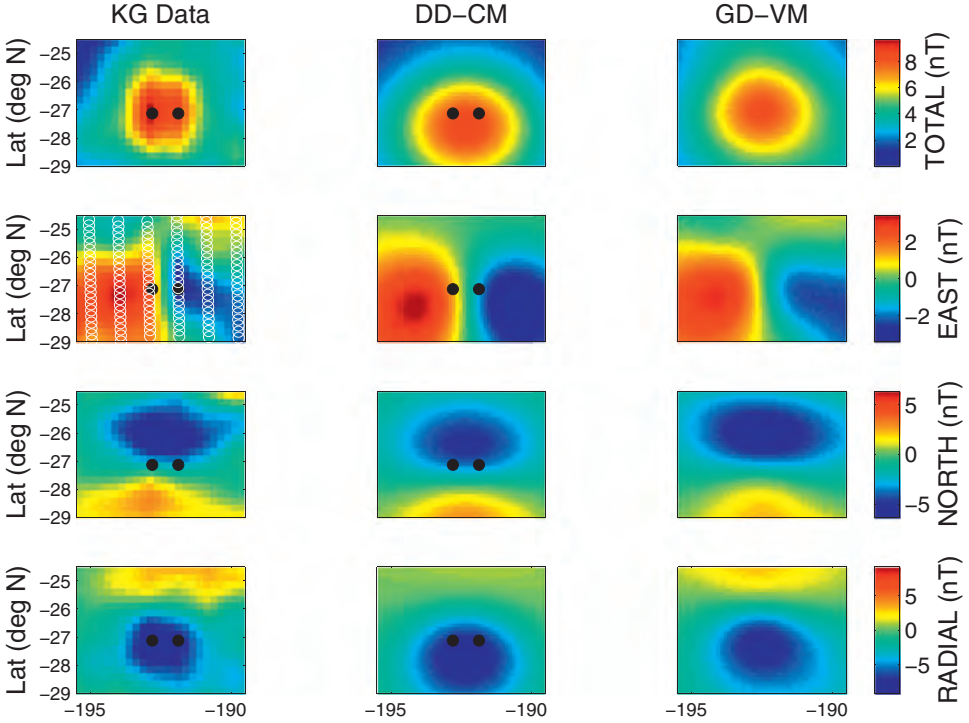

Fig. A8. Area 3 best-fit results for both inversion algorithms. Details are as in Fig. A1, except that the mean measurement altitude is 37.6 km and the observations are from 2009 day 96.

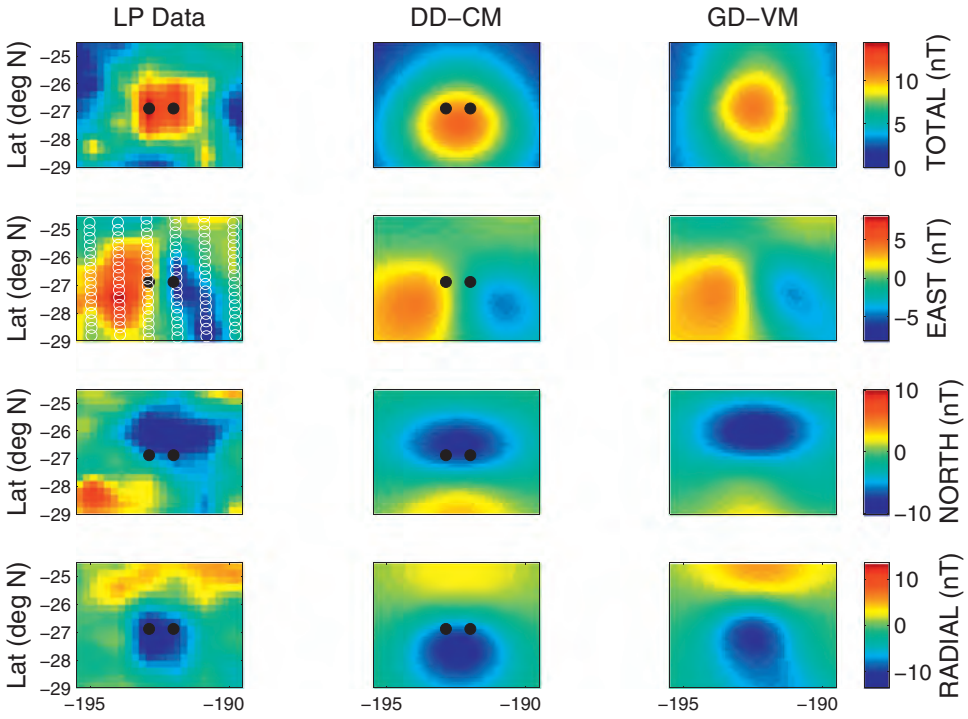

Fig. A9. Area 3 best-fit results for both inversion algorithms. Details are as in Fig. A1, except that the mean measurement altitude is 29.6 km and the observations are from 1999 day 61.

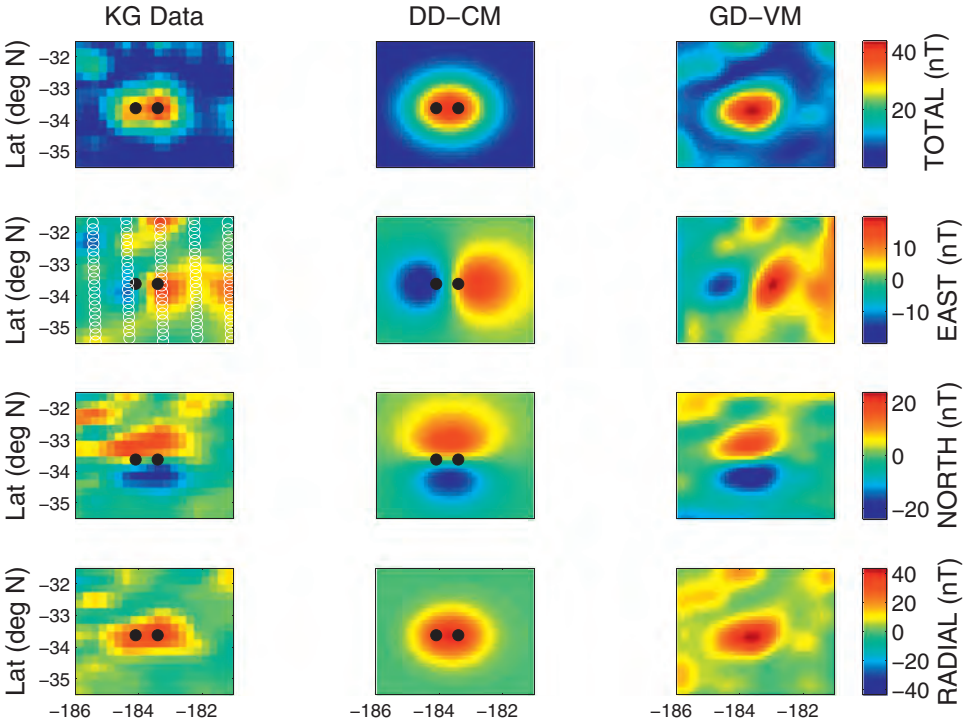

Fig. A10. Area 4 best-fit results for both inversion algorithms. Details are as in Fig. A1, except that the mean measurement altitude is 12.1 km and the observations are from 2009 day 151.

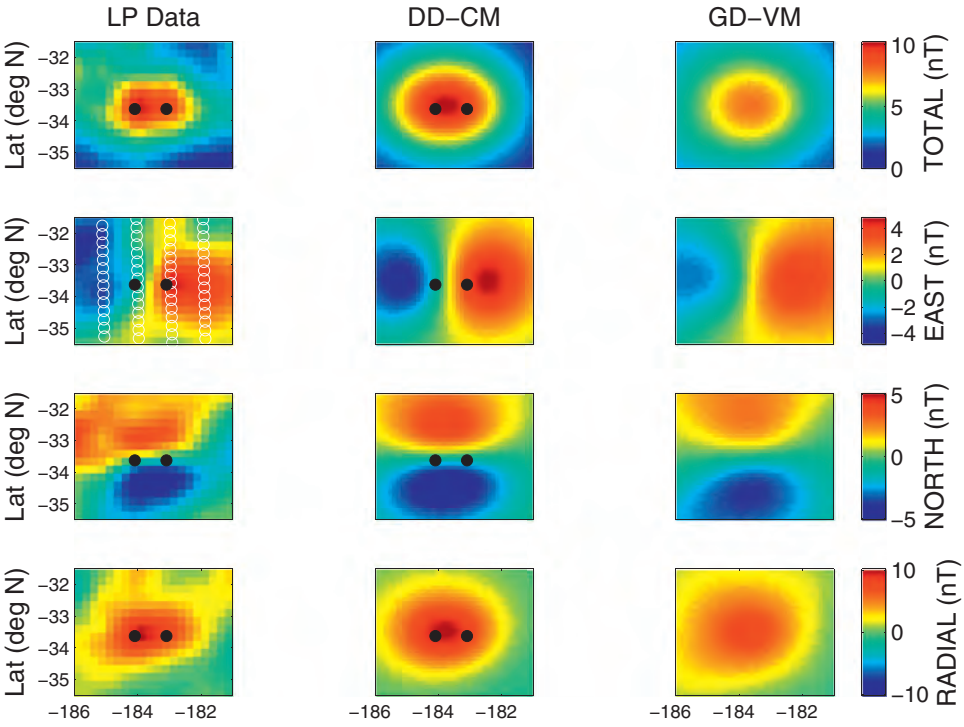

Fig. A11. Area 4 best-fit results for both inversion algorithms. Details are as in Fig. A1, except that the mean measurement altitude is 30.9 km and the observations are from 1999 day 115.

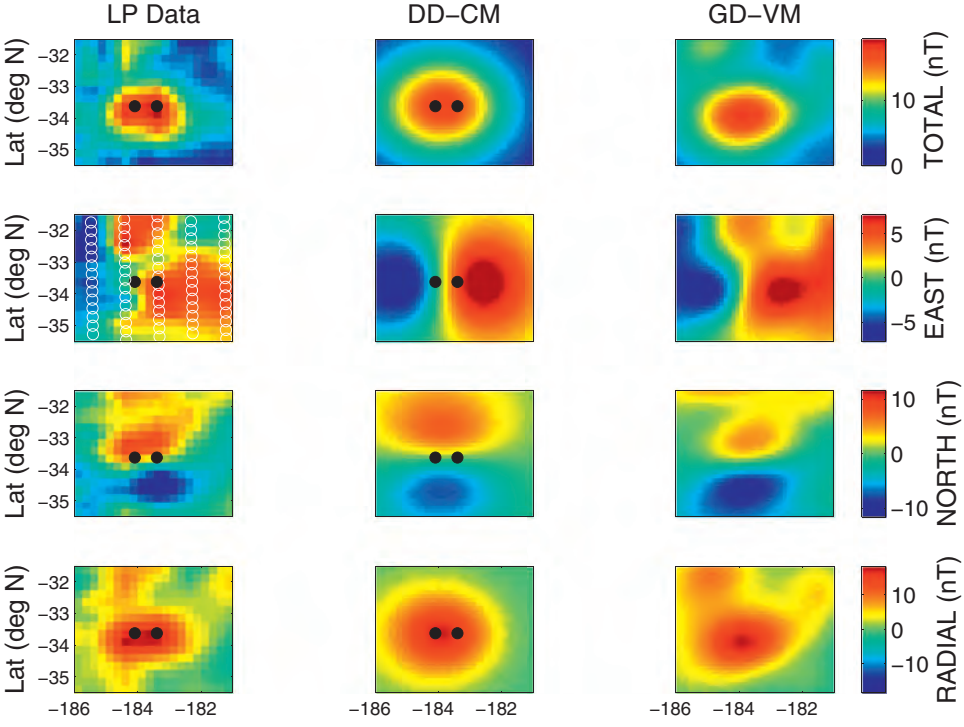

Fig. A12. Area 4 best-fit results for both inversion algorithms. Details are as in Fig. A1, except that the mean measurement altitude is 21.8 km and the observations are from 1999 day 142.

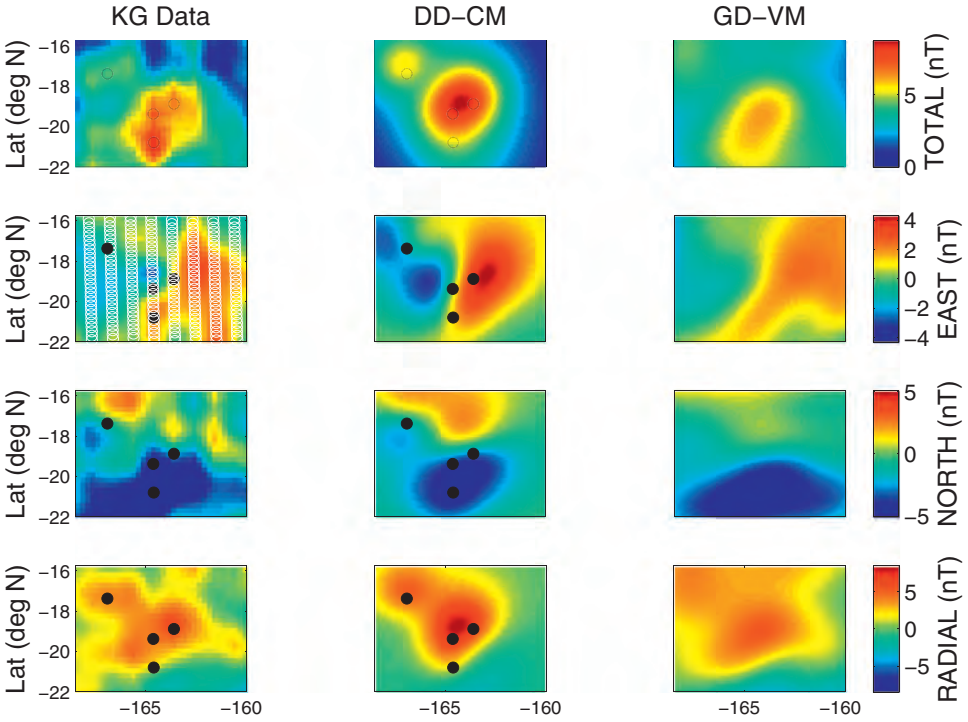

Fig. A13. Area 5 best-fit results for both inversion algorithms. Details are as in Fig. A1, except that the mean measurement altitude is 39.1 km and the observations are from 2009 day 96.

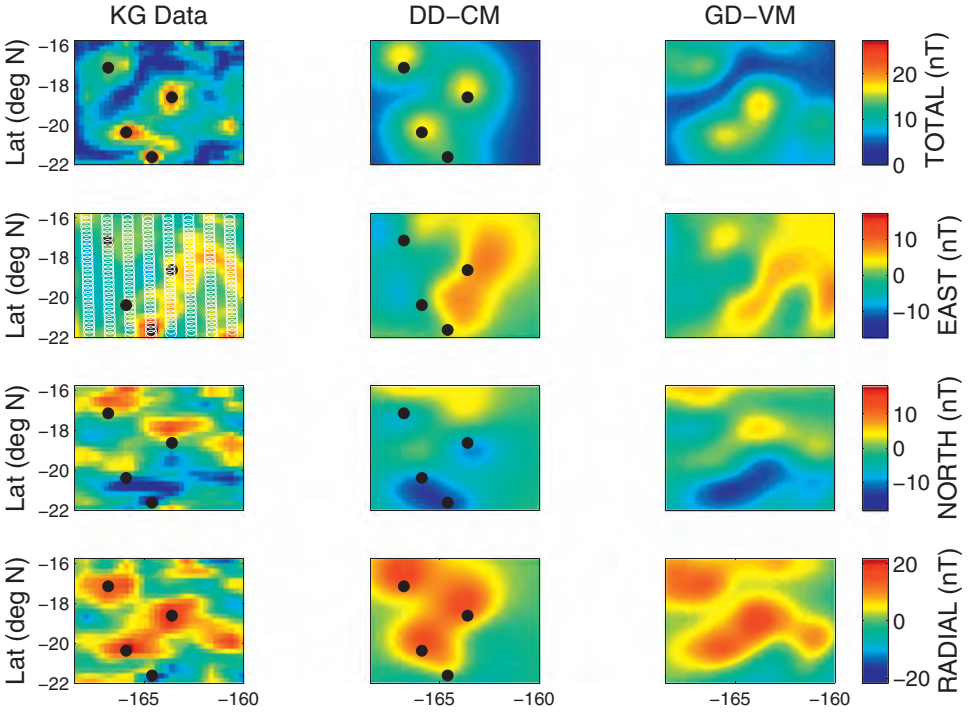

Fig. A14. Area 5 best-fit results for both inversion algorithms. Details are as in Fig. A1, except that the mean measurement altitude is 13.2 km and the observations are from 2009 day 151.

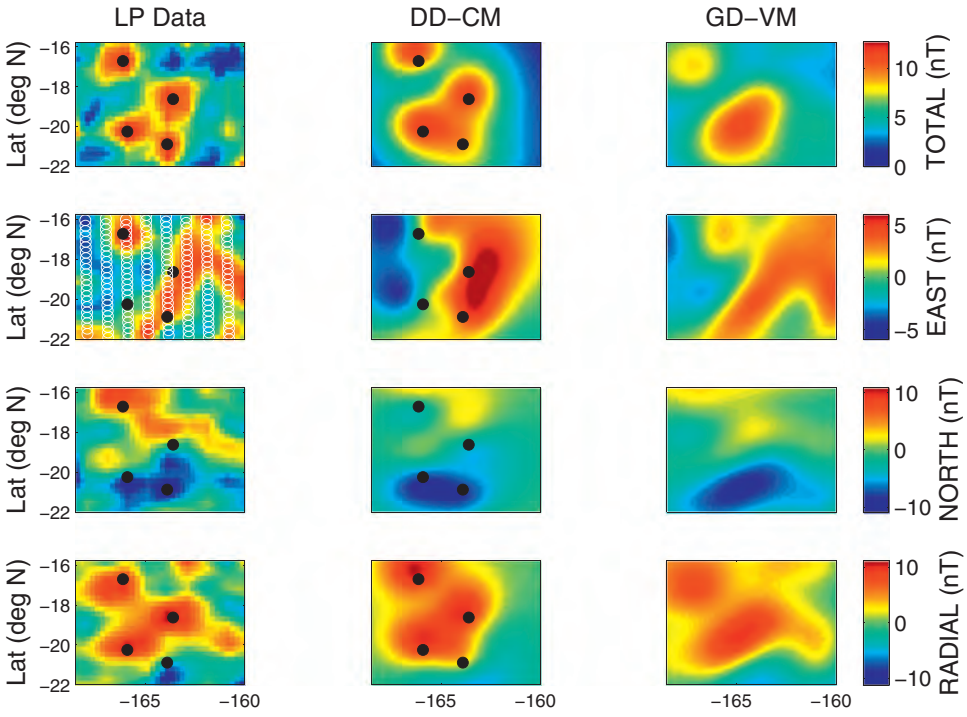

Fig. A15. Area 5 best-fit results for both inversion algorithms. Details are as in Fig. A1, except that the mean measurement altitude is 22.3 km and the observations are from 1999 day 142.

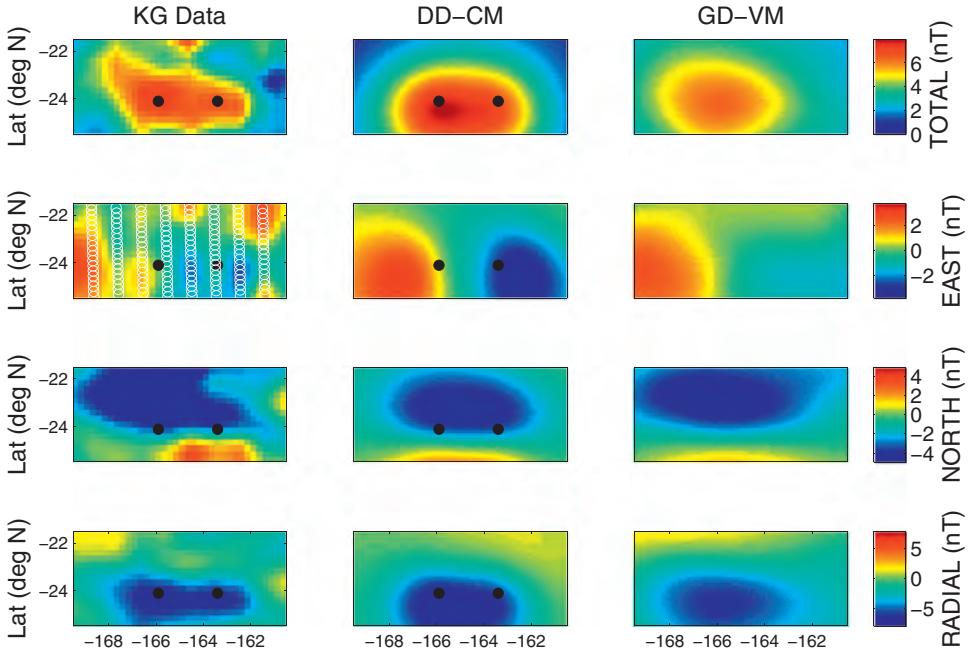

Fig. A16. Area 6 best-fit results for both inversion algorithms. Details are as in Fig. A1, except that the mean measurement altitude is 39.1 km and the observations are from 2009 day 96.

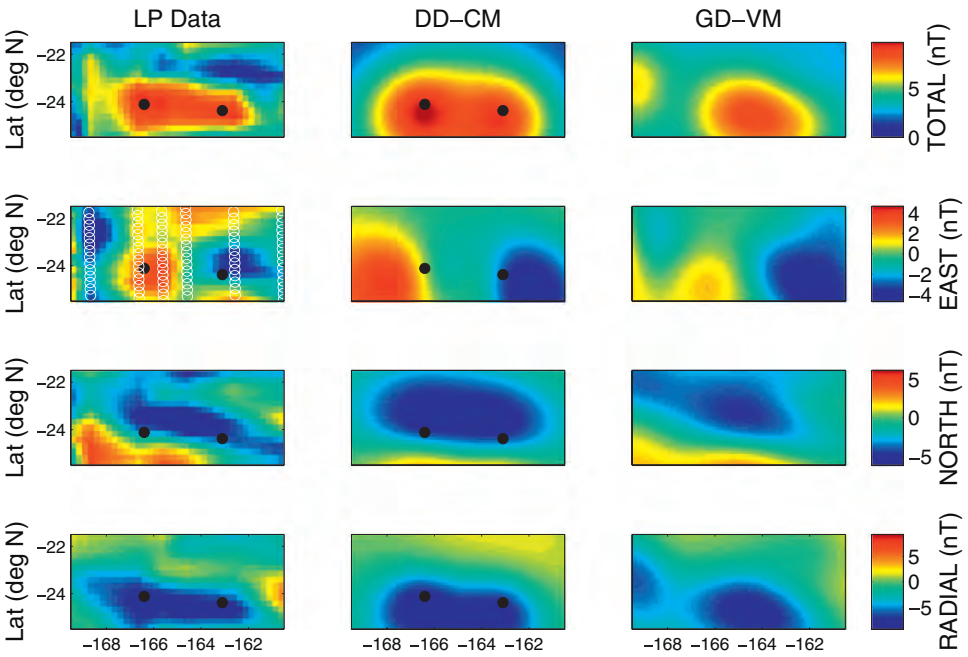

Fig. A17. Area 6 best-fit results for both inversion algorithms. Details are as in Fig. A1, except that the mean measurement altitude is 32.8 km and the observations are from 1999 day 33.

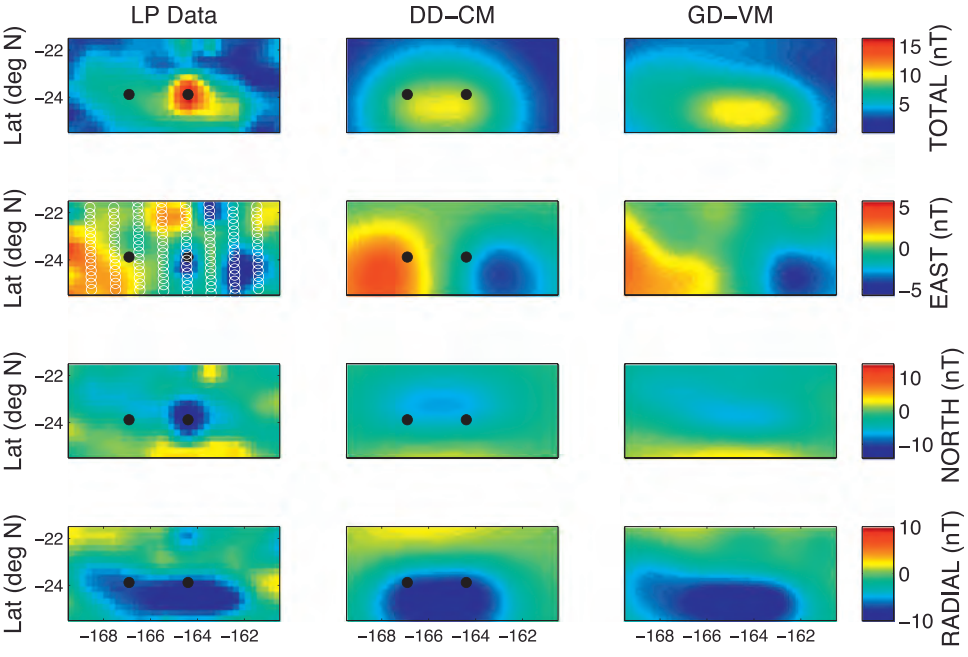

Fig. A18. Area 6 best-fit results for both inversion algorithms. Details are as in Fig. A1, except that the mean measurement altitude is 32.5 km and the observations are from 1999 day 115.

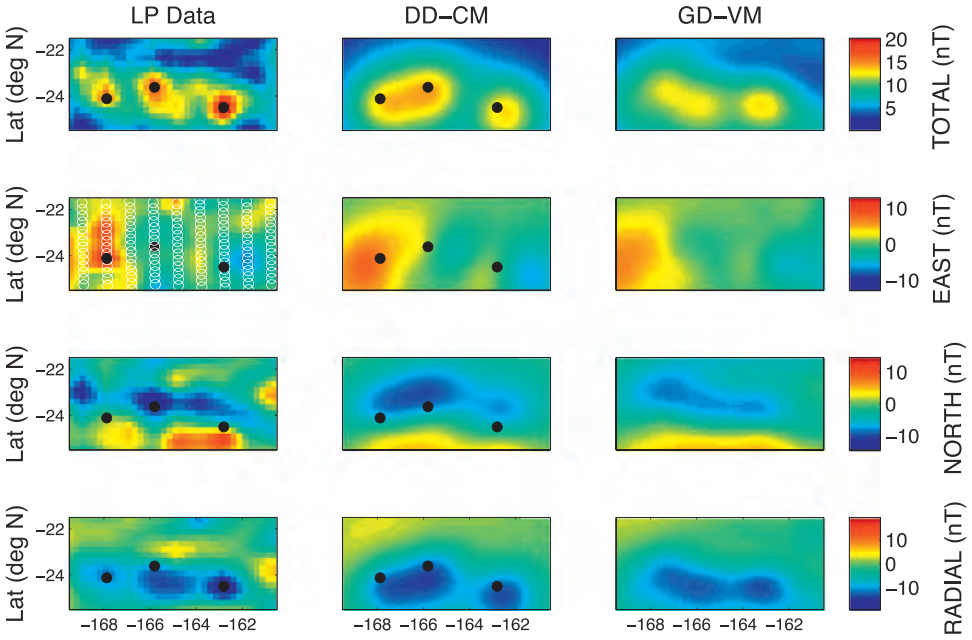

Fig. A19. Area 6 best-fit results for both inversion algorithms. Details are as in Fig. A1, except that the mean measurement altitude is 22.6 km and the observations are from 1999 day 142.

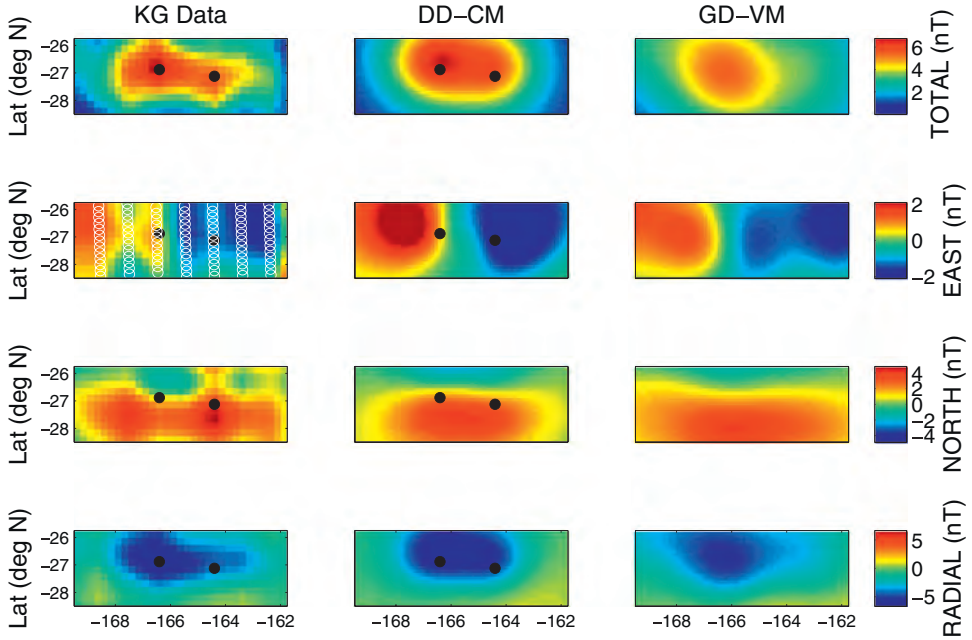

Fig. A20. Area 7 best-fit results for both inversion algorithms. Details are as in Fig. A1, except that the mean measurement altitude is 39.0 km and the observations are from 2009 day 96.

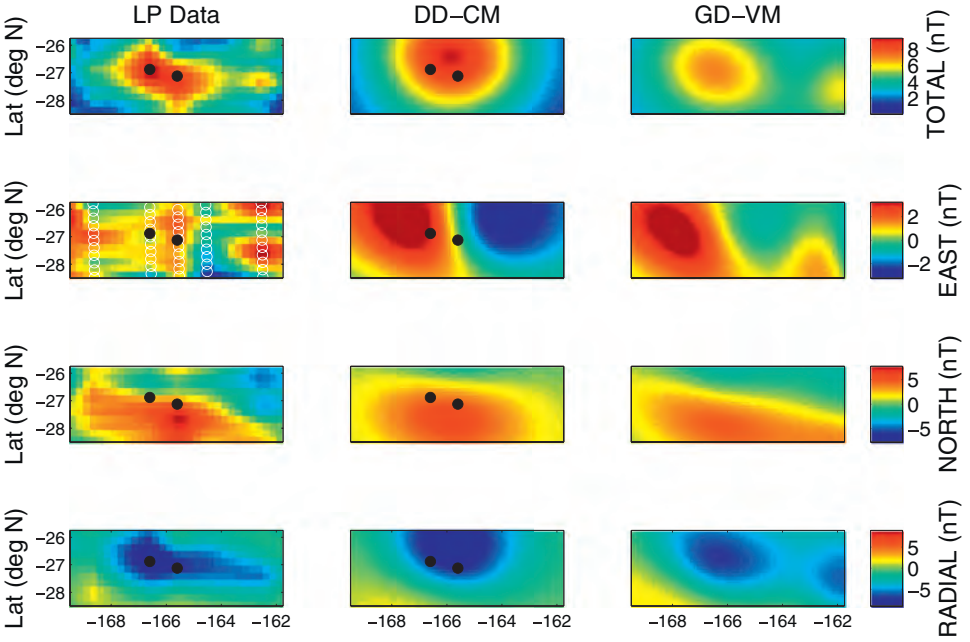

Fig. A21. Area 7 best-fit results for both inversion algorithms. Details are as in Fig. A1, except that the mean measurement altitude is 32.6 km and the observations are from 1999 day 33.

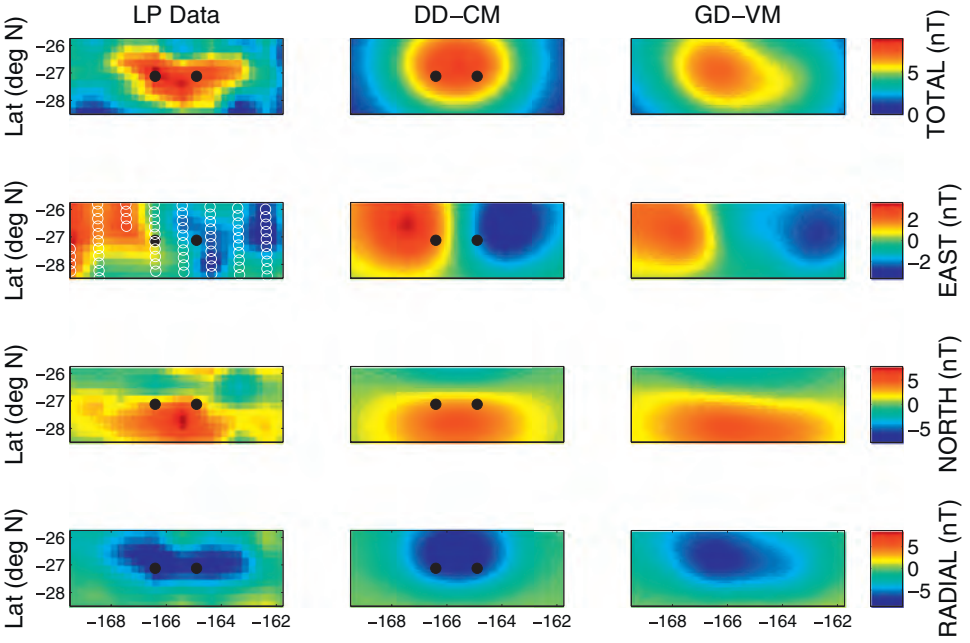

Fig. A22. Area 7 best-fit results for both inversion algorithms. Details are as in Fig. A1, except that the mean measurement altitude is 32.4 km and the observations are from 1999 day 115.

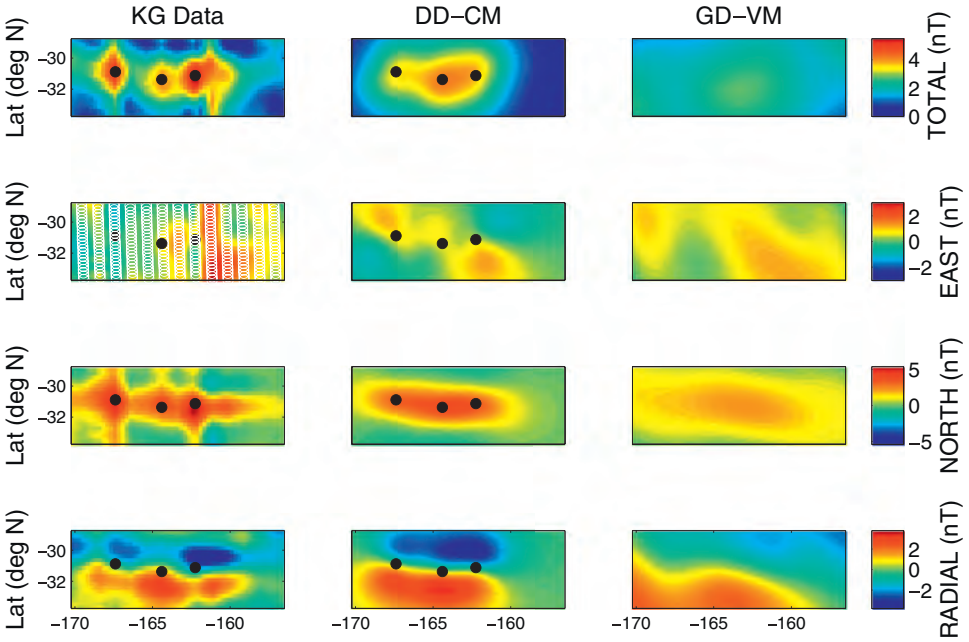

Fig. A23. Area 8 best-fit results for both inversion algorithms. Details are as in Fig. A1, except that the mean measurement altitude is 39.4 km and the observations are from 2009 day 96.

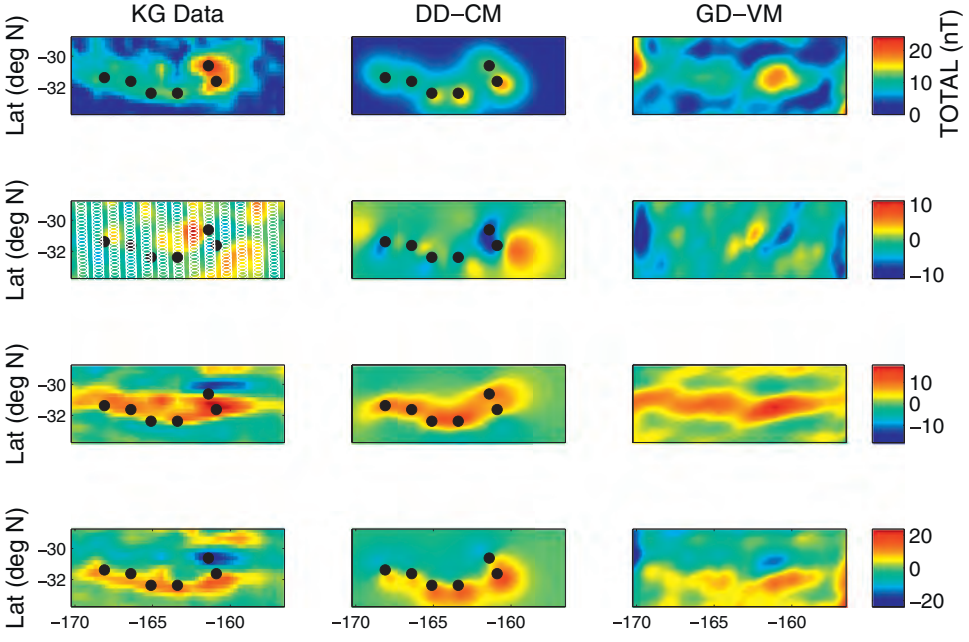

Fig. A24. Area 8 best-fit results for both inversion algorithms. Details are as in Fig. A1, except that the mean measurement altitude is 13.0 km and the observations are from 2009 day 151.

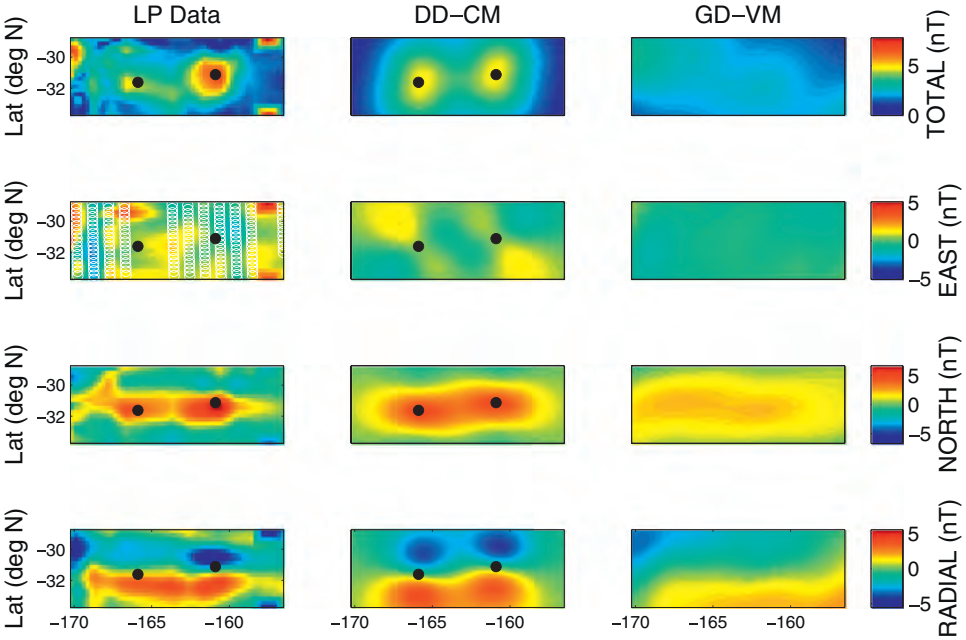

Fig. A25. Area 8 best-fit results for both inversion algorithms. Details are as in Fig. A1, except that the mean measurement altitude is 32.7 km and the observations are from 1999 day 61.

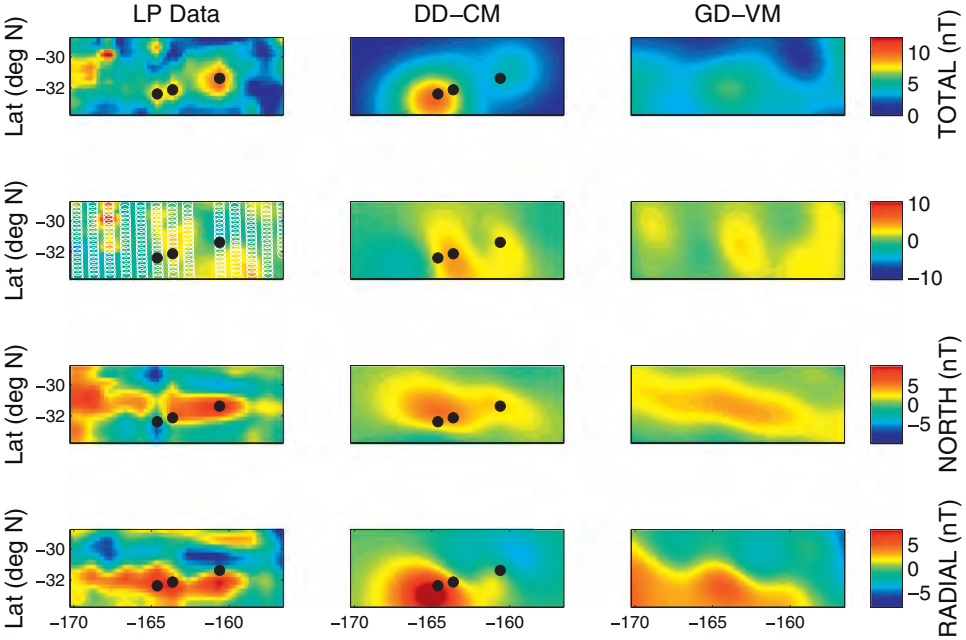

Fig. A26. Area 8 best-fit results for both inversion algorithms. Details are as in Fig. A1, except that the mean measurement altitude is 23.6 km and the observations are from 1999 day 142.

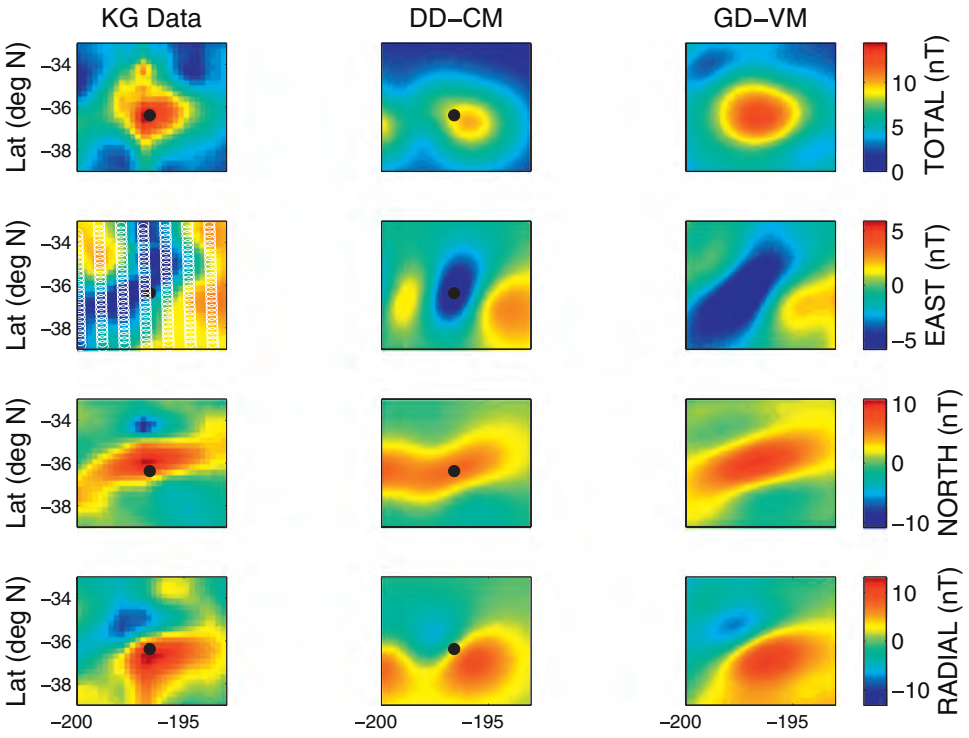

Fig. A27. Area 9 best-fit results for both inversion algorithms. Details are as in Fig. A1, except that the mean measurement altitude is 37.0 km and the observations are from 2009 day 96.

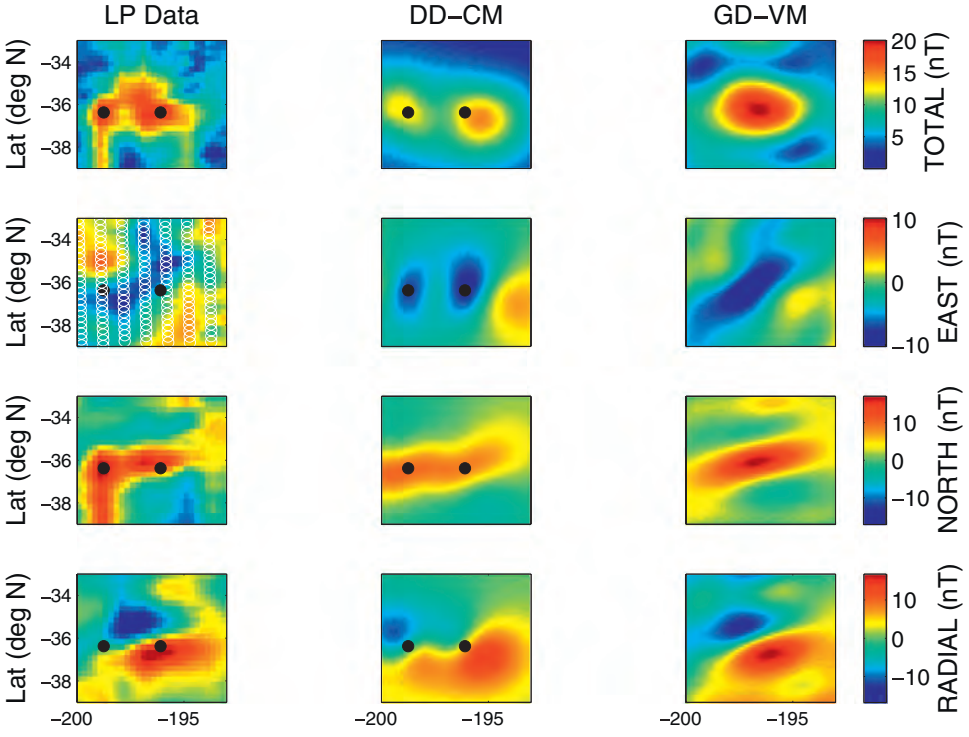

Fig. A28. Area 9 best-fit results for both inversion algorithms. Details are as in Fig. A1, except that the mean measurement altitude is 28.7 km and the observations are from 1999 day 61.

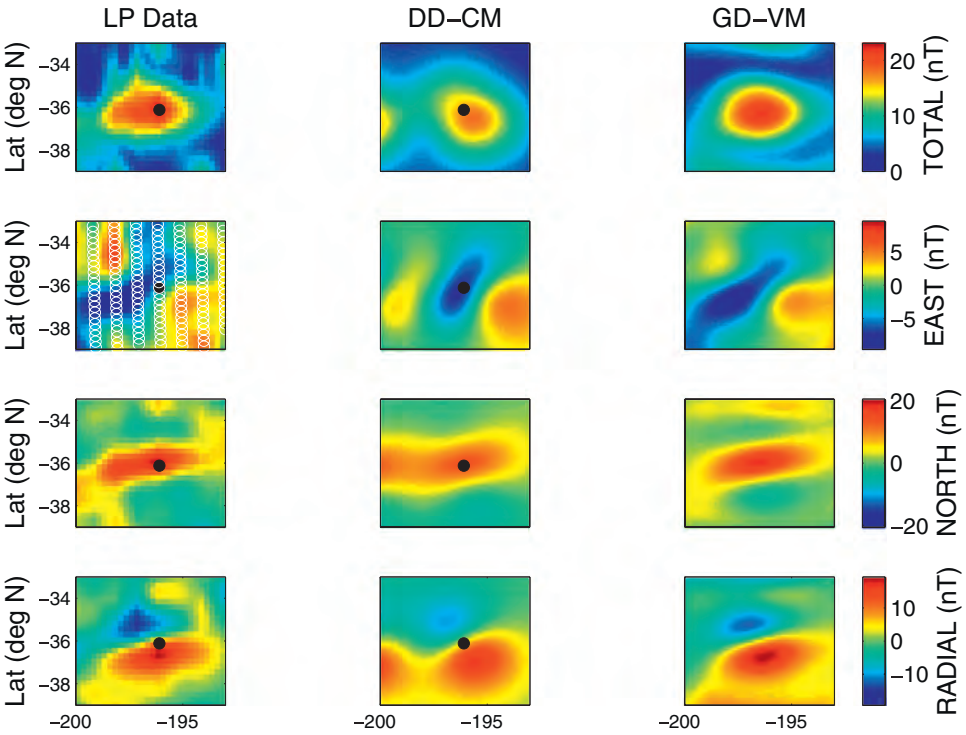

Fig. A29. Area 9 best-fit results for both inversion algorithms. Details are as in Fig. A1, except that the mean measurement altitude is 28.5 km and the observations are from 1999 day 88.

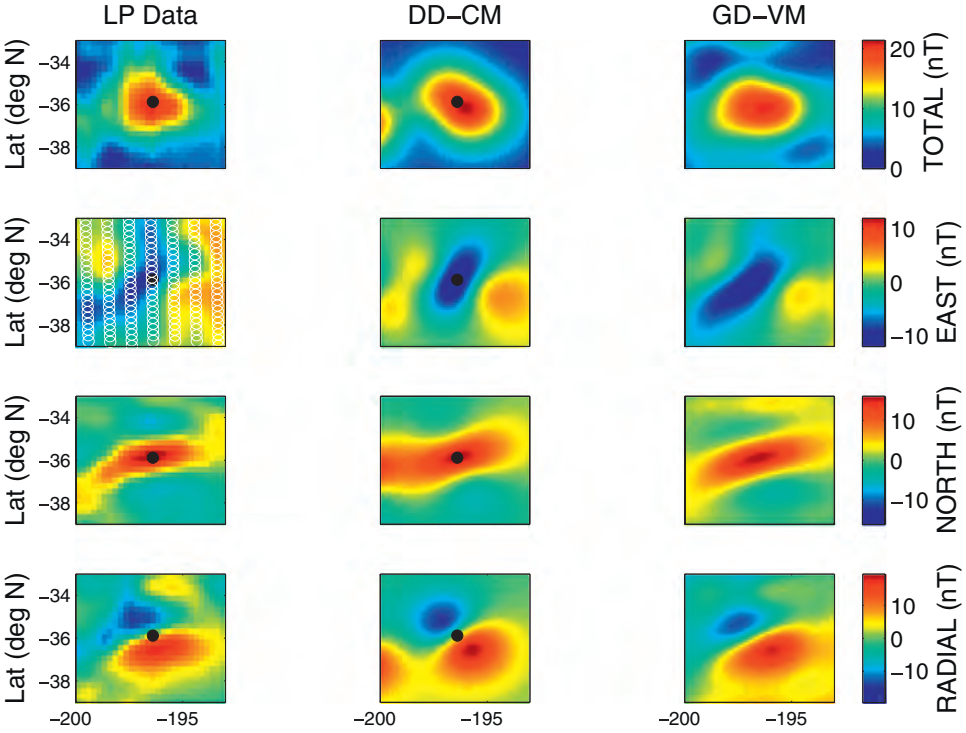

Fig. A30. Area 9 best-fit results for both inversion algorithms. Details are as in Fig. A1, except that the mean measurement altitude is 28.7 km and the observations are from 1999 day 115.

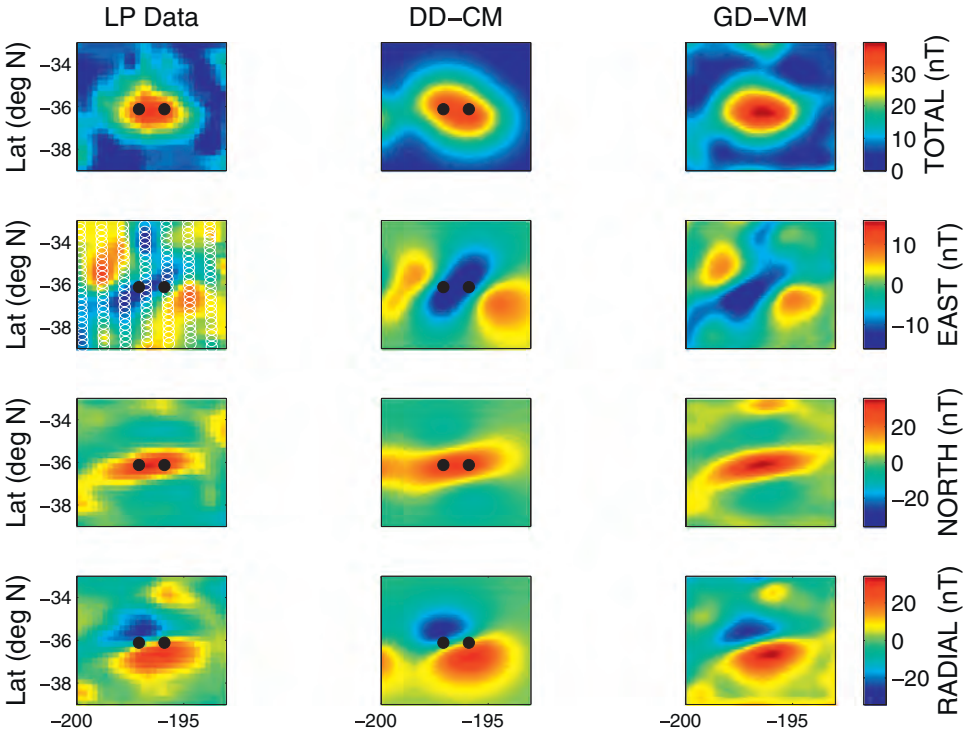

Fig. A31. Area 9 best-fit results for both inversion algorithms. Details are as in Fig. A1, except that the mean measurement altitude is 19.6 km and the observations are from 1999 day 142.

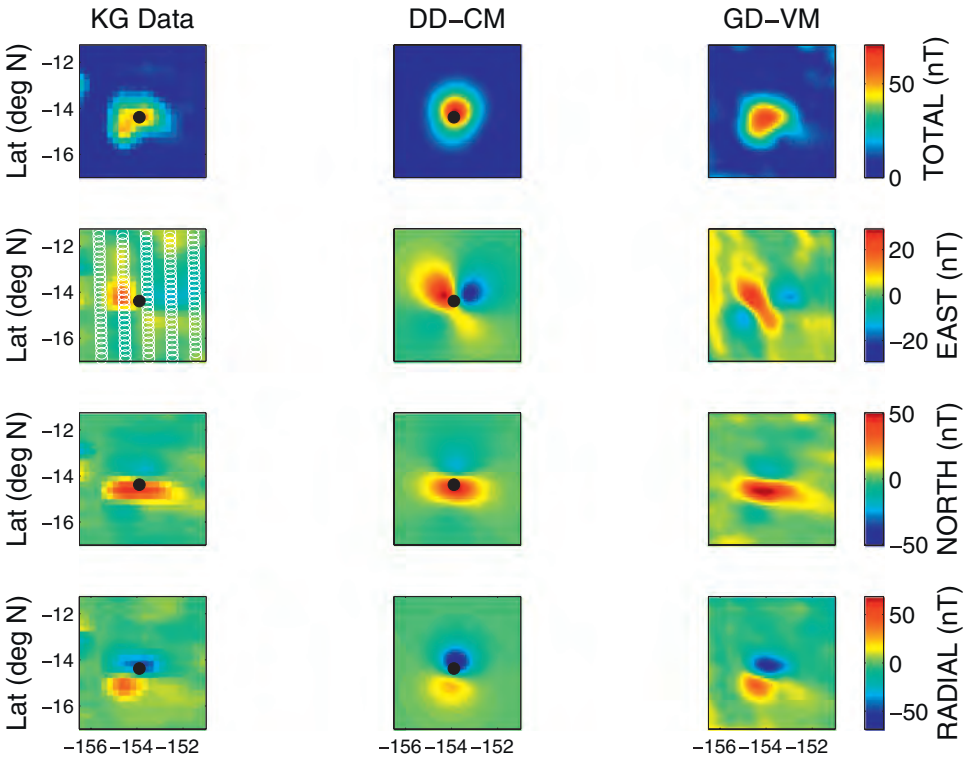

Fig. A32. Area 10 best-fit results for both inversion algorithms. Details are as in Fig. A1, except that the mean measurement altitude is 13.9 km and the observations are from 2009 day 151.

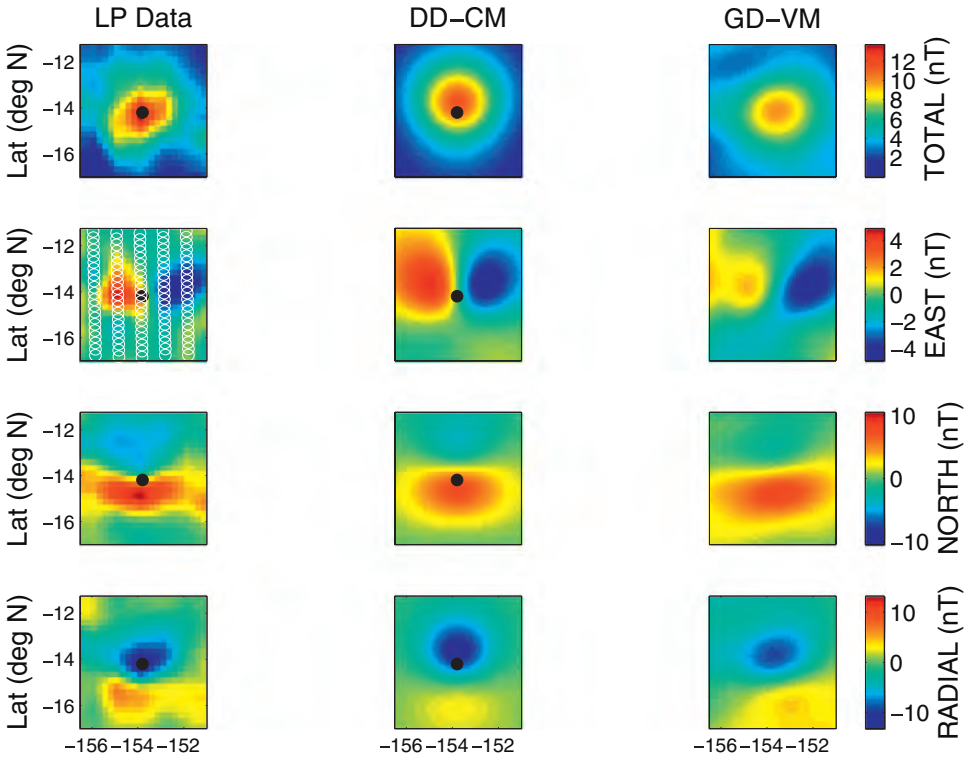

Fig. A33. Area 10 best-fit results for both inversion algorithms. Details are as in Fig. A1, except that the mean measurement altitude is 32.3 km and the observations are from 1999 day 61.

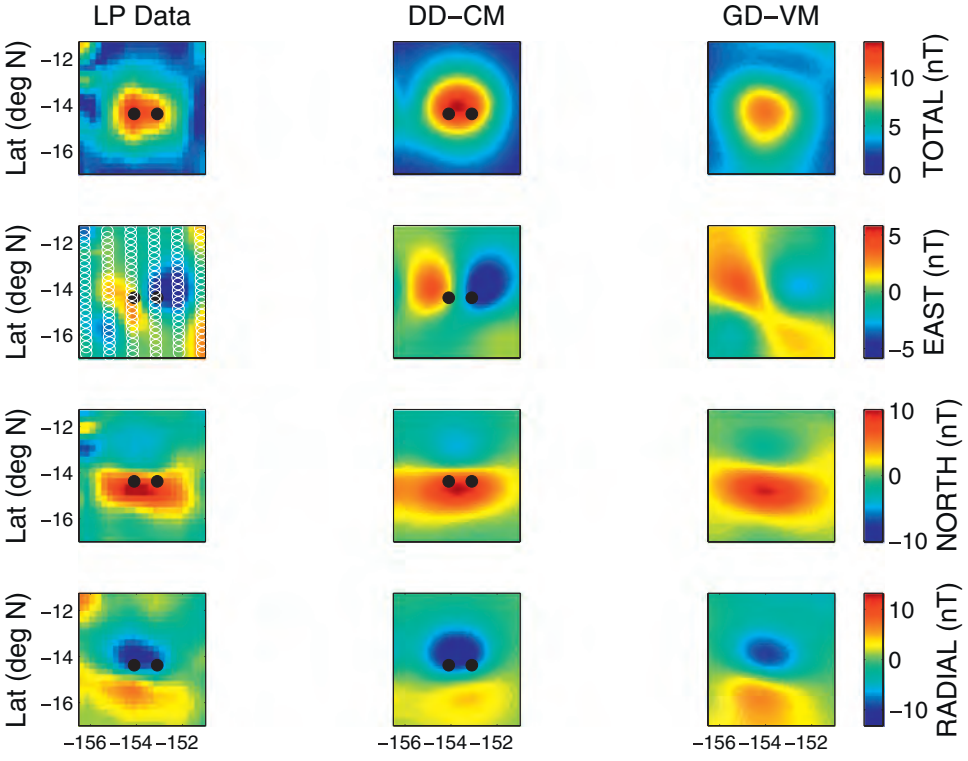

Fig. A34. Area 10 best-fit results for both inversion algorithms. Details are as in Fig. A1, except that the mean measurement altitude is 32.0 km and the observations are from 1999 day 88.

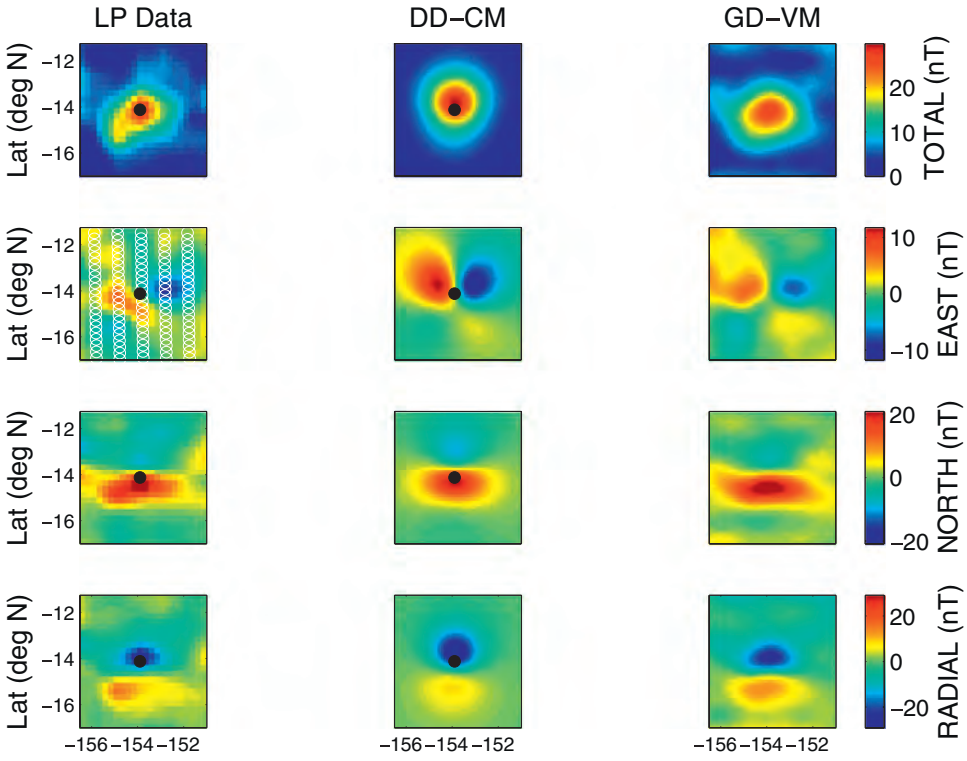

Fig. A35. Area 10 best-fit results for both inversion algorithms. Details are as in Fig. A1, except that the mean measurement altitude is 21.9 km and the observations are from 1999 day 142.

Supplementary materials

Supplementary Appendices B and C can be found, in the online version, at doi:10.1016/j.icarus.2016.09.038.

References

Andrews-Hanna, J.C., Besserer, J., Head III, J.W., Howett, C.J.A., Kiefer, W.S., Lucey, P.J., McGovern, P.J., Melosh, H.J., Neumann, G.A., Phillips, R.J., 2014. Structure and evolution of the lunar Procellarum region as revealed by GRAIL gravity data. Nature 514, 68–71.

Arkani-Hamed, J., Boutin, D., 2014. Analysis of isolated magnetic anomalies and magnetic signatures of impact craters: evidence for a core dynamo in the early history of the Moon. Icarus 237, 262–277. doi:10.1016/j.icarus.2014.04.046.

Arkani-Hamed, J., Olson, P., 2010a. Giant impact stratification of the Martian core. Geophys. Res. Lett. 37. doi:10.1029/2009GL041417.

Arkani-Hamed, J., Olson, P., 2010b. Giant impacts, core stratification, and failure of the Martian dynamo. J. Geophys. Res. 115, E07012. doi:10.1029/2010JE003579.

Arnold, J.R., 1975. Monte Carlo simulation of turnover processes in the lunar regolith. In: Proceedings of the Lunar Planetary Science Conference 6th, pp. 2375–2395.

Blewett, D.T., Coman, E.I., Hawke, B.R., Gillis-Davis, J.J., Purucker, M.E., Hughes, C.G., 2011. Lunar swirls: examining crustal magnetic anomalies and space weathering trends. J. Geophys. Res. 116, E02002. doi:10.1029/2010JE003656.

Butler, R., 1992. Paleomagnetism: Magnetic Domains to Geologic Terranes. Blackwell Scientific Publications, Boston, p. 319.

Coleman, P.J., Schubert, G., Russell, C.T., Sharp, L.R., 1972. Satellite measurements of the Moon's magnetic field: a preliminary report. Moon 4, 419–429. doi:10.1007/BF00562008.

Dwyer, C.A., Stevenson, D.J., Nimmo, F., 2011. A long-lived lunar dynamo driven by continuous mechanical stirring. Nature 479, 212–214. doi:10.1038/nature10564.

Dyal, P., Parkin, C.W., Daily, W.D., 1974. Magnetism and the interior of the Moon. Rev. Geophys. Space Phys. 12. doi:10.1029/RG012i004p00568.

Fisher, R.A. Dispersion on a sphere. Proceedings of the Royal Society of London Series A. 217, 295–305, http://dx.doi.org/10.1098/rspa.1953.0064

Garrick-Bethell, I, 2016. A simple history of lunar true polar wander. 47th Lunar Planetary Science Conference, abstract 2874.

Garrick-Bethell, I., Perera, V., Nimmo, F., Zuber, M.T., 2014. The tidal–rotational shape of the Moon and evidence for polar wander. Nature 512, 181–184. doi:10.1038/nature13639.

Garrick-Bethell, I., Zuber, M.T., 2009. Elliptical structure of the lunar South Pole-Aitken basin. Icarus 204, 399–408. doi:10.1016/j.icarus.2009.05.032.

Gladman, B.J., Burns, J.A., Duncan, M.J., Levison, H.F. The dynamical evolution of lunar impact ejecta. Icarus. 118, 302–321. http://dx.doi.org/10.1006/icar.1995.1193.

Goldreich, P., Toomre, A., 1969. Some remarks on polar wandering. J. Geophys. Res. 74, 2555–2567. doi:10.1029/JB074i010p02555.

Gong, S., Wieczorek, M.A., 2016. Is the lunar magnetic field correlated with gravity or topography? In: 47th Lunar and Planetary Science Conference, abstract 2290.

Halekas, J.S., Brain, D.a., Lin, R.P., Mitchell, D.L., 2008. Solar wind interaction with lunar crustal magnetic anomalies. Adv. Space Res. 41, 1319–1324. doi:10.1016/j.asr.2007.04.003.

Halekas, J.S., Poppe, A., Delory, G.T., Farrell, W.M., Hor, M., 2012. Solar wind electron interaction with the dayside lunar surface and crustal magnetic fields: Evidence for precursor effects. Earth Planets Space 64, 73–82. doi:10.5047/eps.2011.03.008.

Hemingway, D., Garrick-Bethell, I., 2012. Magnetic field direction and lunar swirl morphology: insights from Airy and Reiner Gamma. J. Geophys. Res. 117, E10012. doi:10.1029/2012JE004165.

Hood, L., Williams, C., 1989. The lunar swirls: distribution and possible origins. In: Proceedings of the 19th Lunar Planetary Science Conference, pp. 99–113.

Hood, L., et al., 2011. Initial mapping and interpretation of lunar crustal magnetic anomalies using lunar prospector magnetometer data. J. Geophys. Res. 106, 27825–27839.

Hood, L.L., Artemieva, N.A., 2008. Antipodal effects of lunar basin-forming impacts: initial 3D simulations and comparisons with observations. Icarus 193, 485–502. doi:10.1016/j.icarus.2007.08.023.

Hood, L.L., Huang, Z., 1991. Formation of magnetic anomalies antipodal to lunar impact basins: two dimensional model calculations. J. Geophys. Res. 96, 9837–9846.

Irving, E., 1964. Paleomagnetism and Its Application to Geological and Geophysical Problems, 1st ed.. John Wiley & Sons, Inc, New York, p. 399.

Kramer, G.Y., et al., 2011. Characterization of lunar swirls at Mare Ingenii: a model for space weathering at magnetic anomalies. J. Geophys. Res. 116, E04008. doi:10.1029/2010JE003669.

Kurata, M., Tsunakawa, H., Saito, Y., Shibuya, H., Matsushima, M., Shimizu, H., 2005. Mini-magnetosphere over the Reiner Gamma magnetic anomaly region on the Moon. Geophys. Res. Lett. 32, L24205. doi:10.1029/2005GL024097.

Le Bars, M., Wieczorek, M.A., Karatekin, Ö., Cébron, D., Laneuville, M., 2011. An impact-driven dynamo for the early Moon. Nature 479, 215–218. doi:10.1038/nature10565.

Lin, R.P., et al., 1998. Lunar surface magnetic fields and their interaction with the solar wind: results from lunar prospector. Science 281, 1480–1484. doi:10.1126/science.281.5382.1480.

Mitchell, D.L., et al., 2008. Global mapping of lunar crustal magnetic fields by Lunar Prospector. Icarus 194, 401–409. doi:10.1016/j.icarus.2007.10.027.

Nayak, M., Nimmo, F., Udrea, B., 2016. Effects of mass transfer between Martian satellites on surface geology. Icarus 267, 220–231. doi:10.1016/j.icarus.2015.12.026.

Nayak, M.V, Asphaug, E., 2016. Sesquinary Catenae on the Martian satellite phobos from reaccretion of escaping ejecta. Nat. Commun. 7, 12591. doi:10.1038/NCOMMS12591.

Nicholas, J.B., Purucker, M.E., Sabaka, T.J., 2007. Age spot or youthful marking: Origin of Reiner Gamma. Geophys. Res. Lett. 34, L02205. doi:10.1029/2006GL027794.

Parker, R.L., 1988. A statistical theory of seamount magnetism. J. Geophys. Res. 93, 3105–3115. doi:10.1029/JB093iB04p03105.

Parker, R.L., 1991. A theory of ideal bodies for seamount magnetism. J. Geophys. Res. 96, 16101–16112. doi:10.1029/91JB01497.

Peale, S.J., 1976. Excitation and relaxation of the wobble, precession, and libration of the Moon. J. Geophys. Res. 81, 1813–1827. doi:10.1029/JB081i011p01813.

Purucker, M.E., 2008. A global model of the internal magnetic field of the Moon based on lunar prospector magnetometer observations. Icarus 197, 19–23. doi:10.1016/j.icarus.2008.03.016.

Purucker, M.E., Head, J.W., Wilson, L., 2012. Magnetic signature of the lunar South Pole-Aitken basin: character, origin, and age. J. Geophys. Res. 117, E05001. doi:10.1029/2011JE003922.

Purucker, M.E., Nicholas, J.B., 2010. Global spherical harmonic models of the internal magnetic field of the Moon based on sequential and coestimation approaches. J. Geophys. Res. 115, E12007. doi:10.1029/2010JE003650.

Runcorn, S.K., 1983. Lunar magnetism, polar displacements and primeval satellites in the Earth–Moon system. Nature 304, 589–596. doi:10.1038/304589a0.

Siegler, M.A., et al., 2016. Lunar true polar wander inferred from polar hydrogen. Nature 531, 480–484. doi:10.1038/nature17166.

Smith, D.E., et al., 2010. Initial observations from the lunar orbiter laser altimeter (LOLA). Geophys. Res. Lett. 37, 1–6. doi:10.1029/2010GL043751.

Takahashi, F., Tsunakawa, H., Shimizu, H., Shibuya, H., Matsushima, M., 2014. Reorientation of the early lunar pole. Nat. Geosci. 7, 409–412. doi:10.1038/ngeo2150.

Tsunakawa, H., Takahashi, F., Shimizu, H., Shibuya, H., Matsushima, M., 2014. Regional mapping of the lunar magnetic anomalies at the surface: method and its application to strong and weak magnetic anomaly regions. Icarus 228, 35–53. doi:10.1016/j.icarus.2013.09.026.

Weiss, B.P., Tikoo, S.M., 2014. The lunar dynamo. Science 346, 1198. doi:10.1126/science.1246753.

Wieczorek, M.A., Weiss, B.P., 2010. Testing the lunar dynamo hypothesis using global magnetic field data. 41st Lunar and Planetary Science Conference, abstract 1625.

Wieczorek, M.A., Weiss, B.P., Stewart, S.T., 2012. An impactor origin for lunar magnetic anomalies. Science 335, 1212–1215. doi:10.1126/science.1214773.

Williams, J., Boggs, D., Yoder, C.F., Ratcliff, J.T., Dickey, J.O., 2001. Lunar rotational dissipation in solid body and molten core. J. Geophys. Res. 106, 27933–27968. doi:10.1029/2000JE001396.

Zahnle, K., Alvarellos, J.L., Dobrovolskis, A., Hamill, P., 2008. Secondary and sesquinary craters on Europa. Icarus 194, 660–674. doi:10.1016/j.icarus.2007.10.024.

Zuber, M.T., et al., 2013. Gravity field of the Moon from the gravity recovery and interior laboratory (GRAIL) mission. Science 339, 668–671. doi:10.1126/science.1231507.